Scenario for the onset of space-time chaos

Gilad Goren,[1] Jean-Pierre Eckmann,[1,2] and Itamar Procaccia[1]
[1]*Department of Chemical Physics, The Weizmann Institute of Science, Rehovot 76100, Israel*
[2]*Department of Theoretical Physics and Department of Mathematics, University of Geneva, 1211 Geneva 4, Switzerland*
(Received 31 March 1997; revised manuscript received 23 December 1997)

The onset of space-time chaos is studied on the basis of a Galilean invariant model that exhibits the essential characteristics of the phenomenon. By keeping the linear part of the model extremely simple, one has better than usual control of the classes of available stationary solutions. These stationary solutions include not only spatially periodic but also a large set of spatially chaotic solutions that can be characterized by words of a symbolic language. The main proposition of this paper is that space-time chaos in Galilean invariant models can be understood in a qualitative fashion as an orbit in the space of functions that visits words in this language in a random fashion. The appearance of topological defects and other ''signatures'' of space-time chaos are a natural consequence of this dynamics. Finally, we construct a simple demonstration of this scenario. [S1063-651X(98)07204-3]

PACS number(s): 05.45.+b

I. INTRODUCTION

The study of space-time chaos is hampered by the fact that it is a phenomenon that appears in systems described by partial differential equations (PDEs). In comparison, temporal chaos is adequately described by ordinary differential equations. For the latter there is a well-established qualitative theory that forms a convenient and solid basis for the description of temporal chaos. The lack of a qualitative theory of PDEs confined much of the theoretical work on space-time chaos to numerical simulations of model equations. Even though there has been much progress in relating basic symmetries of physical systems to the type of model equations that need to be studied (''normal forms''), the actual understanding of the onset of space-time chaos and the characterization of what happens after the onset did not exceed a descriptive mode. Signatures of space-time chaos, such as topological defects and disordered cellular patterns, became surrogate to the phenomenon itself, with descriptions such as ''defect mediated turbulence'' [1] and ''spatiotemporal intermittency'' [2].

Popular models to analyze space-time chaos have been the Ginzburg-Landau and the Kuramoto-Sivashinsky equations. Some important work has been done to map the dynamical behavior in such models and to discuss the existence of attractors. Examples of such work can be found, e.g., in [3–5]. The main difficulty in understanding the onset of space-time chaos is that even these relatively simple equations lead to such a huge variety of phenomena that it is hard to disentangle clean scenarios. Typically there is such a complex array of dynamical phenomena that appear concurrently that they tend to obscure the essential issues related to space-time chaos. Even the definition of space-time chaos is not entirely obvious. In some sense, the simplest models that have been used are too complicated. It becomes necessary to simplify further with the hope that such a simplification would lead to more feasible analysis.

The main aim of this paper is to propose such simplified models. We will construct a model that enjoys the same symmetries as some of the popular models of space-time chaos, but whose analytic structure is sufficiently simple to allow a reasonable understanding of the classes of solutions that are available. This will allow us to classify families of stationary and time-dependent solutions. More importantly, we will develop a picture that describes how the orbit in function space visits these solutions much like hyperbolic fixed points are visited in low-dimensional dynamical systems. What comes out is thus a qualitative picture of the onset of space-time chaos and an understanding of how some of the signatures of this type of chaos appear as a consequence of the dynamics in function space. In some sense the emerging picture is reminiscent of phase-space orbits of dynamical systems, with the stationary and the time-periodic solutions being organizers of complex behavior. We believe that similar pictures are available in standard models of space-time chaos with the same symmetries, but they are harder to discern because of the higher degree of complexity. The structure of this paper is as follows. In Sec. II we present the model that will be discussed in the rest of the paper. After specifying the essential symmetries and features of the dynamics, we propose a generalized equation that reflects all these properties but which has only one or two linearly unstable modes. Although infinitely many modes appear in the observed dynamics, the simplicity of the linear operator is the key to our ability to develop a deeper understanding. In Sec. III we begin the discussion of the stationary solutions of our model. The aim is to understand as many stationary solutions as possible since later we describe the dynamics as being organized by these stationary solutions. In Sec. III we focus on the family of solutions whose typical wavelength is much smaller than the size of the system. We show that there is an infinity of such solutions and that they can be organized with the help of a symbolic grammar. With this device we demonstrate that the system has spatial positive topological entropy in the sense that the number of available stationary solutions increases at least exponentially with the size of the system. After some analysis of the spatial bifurcations of these stationary solutions we turn in Sec. IV to the discussion of a family of solutions whose typical wavelength is of the order of the system size. We find two solutions in this family

and we discuss their stability under temporal perturbations. This stability analysis calls for some special tricks since there exist infinitely many modes that are marginally stable. From the conceptual point of view of describing spatiotemporal chaos, Sec. V is the central section of this paper. It attempts to offer a comprehensive picture of the dynamics in qualitative terms using the knowledge of the stationary solutions and monitoring the orbit that moves between them in function space. In some sense the emerging picture is a generalization to function space of the common picture in low-dimensional dynamical systems. To demonstrate these ideas, we construct a simple example in which it is easy to identify the spatial structures that are being revisited by the temporal solution. It is possible to track a series of bifurcations that connect the basins of attraction of temporally unstable solutions of the type discussed in Secs. II–IV.

II. MODEL

One of the important insights achieved in the study of space-time chaos is that given some symmetries, the dynamics of the physical fields, after appropriate scaling, is described by universal equations. The structure of the equations is completely determined by the symmetries of the physical system. In this paper we will be concerned with model equations in one spatial dimension that respect four symmetries: translation in time ($t\rightarrow t+\tau$), translation in space ($x\rightarrow x+a$), parity [$U(x,t)\rightarrow -U(-x,t)$], and Galilean symmetry

$$U(x,t)\rightarrow U(x+ct,t)+c. \tag{2.1}$$

A general form of a dissipative, first order in time, sourceless scalar field model that obeys these symmetries is

$$\partial_t U(x,t)=\mathcal{L}[U(x,t)]+\mathcal{N}[U(x,t)],$$
$$(x,t)\in \mathbb{R}^1\times\mathbb{R}_+, \tag{2.2}$$

where the nonlinear operator is

$$\mathcal{N}[U(x,t)]\equiv U(x,t)\partial_x U(x,t). \tag{2.3}$$

The linear operator $\mathcal{L}[\ ]$ can be represented in the function space of its eigenmodes $\hat{e}_k(x)$. We denote this function space by $\mathcal{U}$ and a vector in $\mathcal{U}$ by $U(k)$ (where the index k takes on discrete or continuous values; also see below). The spectrum of the linear operator is denoted by $L(k)$:

$$\mathcal{L}[\hat{e}_k(x)]=L(k)\hat{e}_k(x). \tag{2.4}$$

A solution (orbit) in function space will be the time-dependent vector

$$U(k,t)=\int dx\, U(x,t)\hat{e}_k^*(x), \tag{2.5}$$

where the asterisk denotes the complex conjugate. The operation of the linear operator in real space is expressed by

$$\mathcal{L}[U(x,t)]=\int dk\, dy\, \hat{e}_k(x)L(k)U(y,t)\hat{e}_k^*(y). \tag{2.6}$$

The four symmetries place restrictions on the possible forms of the linear operator. We choose the eigenfunctions of the translation operator as the basis for the function space $\mathcal{U}$. A sufficient condition for the linear operator to ensure Galilean symmetry is

$$L(0)=0 \tag{2.7}$$

and parity requires

$$L(-k)=L(k). \tag{2.8}$$

We also require $U(x,t)$ to be a real field. In this paper $\mathcal{L}[\ ]$ is purely dissipative so $L(k)$ is a real operator. This class of nonlinear models conserves antisymmetry and our study is restricted to the subspace of odd functions with periodic boundary conditions

$$U(x+\mathfrak{L},t)=U(x,t), U(x,t)=-U(-x,t). \tag{2.9}$$

In order to have a nonvanishing solution for any time t, one needs either external forcing or unstable modes (positive eigenvalues) in the linear spectrum to inject energy into the system and stable modes (negative eigenvalues) to dissipate energy and stabilize the solution. In this paper we will not discuss models with external forcing, so the models that we are interested in must have unstable and stable bands. We fix the scaling in k space such that the boundary between the two bands is positioned at $k=1$. Two additional length scales appear in the problem: (i) the system size $\mathfrak{L}$ or the k-space grid size $\Delta k=2\pi/\mathfrak{L}$ and (ii) $k_{\max}$ or the real-space grid size $\Delta x=\pi/k_{\max}$.

Known models of the class discussed above are the Michelson-Sivashinsky equation [$L(k)=|k|-k^2$] and the Kuramoto-Sivashinsky equation [$L(k)=k^2-k^4$]. The Kuramoto-Sivashinsky equation is a well-known example possessing ordered and spatially chaotic states [4,6–8]. The spatiotemporally chaotic state is characterized using two different languages. In the statistical approach one characterizes this state by its long-wavelength average spectrum [5,9]. The other approach looks at the short-wavelength cellular structure [$k\sim O(1)$] and at the topological defects that appear together with the ordered structure. These two descriptions express two aspects of one single phenomenon. Any attempt to understand space-time chaos should deal with both branches of the spatial spectrum.

The analysis of the Kuramoto-Sivashinsky equation is complicated for two reasons. Owing to the large number of unstable modes [$\sim O(\mathfrak{L})$] [10,11] the space-time picture seems stochastic with complex dynamics that involves tip splitting (in one spatial dimension) or creation and annihilation of topological defects (in higher dimensions). The second reason is the lack of controlled transition from the ordered phase to space-time chaos. The only control parameter of the Kuramoto-Sivashinsky equation is the system size $\mathfrak{L}$.

In order to have control over a system with many degrees of freedom we decide to generalize the possible linear operators $\mathcal{L}[\ ]$ to include integro-differential operators, i.e., we relax the demand of locality in space. We suggest and study a model with only two linearly unstable modes as a simplified model that contains the important features of the Kuramoto-Sivashinsky equation. In this model only two spatial modes

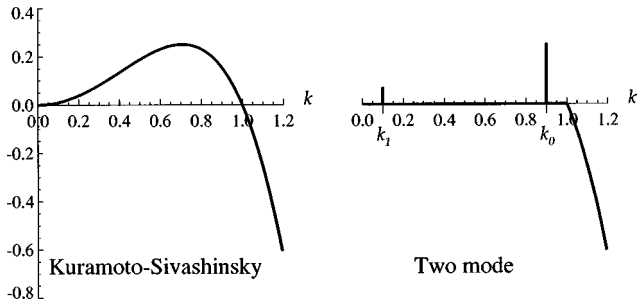

FIG. 1. Linear spectrum of two Galilean invariant models.

at the two extremes of the unstable band are unstable, while all other modes in the unstable band $|k|<1$ are marginal (see Fig. 1). In other words,

$$L(k)=\begin{cases}\alpha\delta(|k|-k_0)+\beta\delta(|k|-k_1) & \text{if } |k|<1 \quad (k_1\ll k_0)\\ k^2-k^4 & \text{if } |k|\geqslant 1.\end{cases} \tag{2.10}$$

This model has three principal control parameters: α, β, and the minimal wave number Δk or the system size $\mathfrak{L}$. One control parameter (α) gives us control over the short-wavelength part of the spectrum of the solutions of the model, while the other control parameter (β) enables us to control the long-wavelength part of the spectrum. In the following sections we will show how by varying the control parameters the model (2.2) and (2.10) exhibits ordered patterns, spatial chaos, temporal chaos, and space-time chaos. Throughout the text we will point out similarities between solutions of our model and of other Galilean invariant models.

III. A FAMILY OF STATIONARY SOLUTIONS OF THE FIRST KIND

Any study of a dynamical system should start with an analysis of its fixed points, and in our case, these are the stationary solutions. The first family of stationary solutions that we discuss depends mainly on the value of the parameter α. Qualitatively all these solutions have strong spectral components with $k=k_0$ and its subharmonics. To understand the nature of the solutions in this family we begin with the analysis of the simplest solution of this type. This type of solution has already been discovered in the context of the Kuramoto-Sivashinsky equation [7], but there one has a band of such solutions.

A. The cellular solution

Consider a long-wavelength ($k\sim k_0$) periodic cellular solution of model (2.2) and (2.10) of the form

$$U_h(x)=\sum_{n\neq 0} ia_n e^{ink_0x}, \quad a_{-n}=-a_n^*. \tag{3.1}$$

(Because of the Galilean symmetry we may take $a_0=0$.) When Eq. (3.1) is substituted into the model equation, an infinite set of coupled nonlinear algebraic equations is generated. To enable analytic calculations, we reduce the number of degrees of freedom in order to find an approximate solution to this set of equations. We anticipate that the amplitudes of the linearly stable modes decay exponentially with their spatial frequency, and by disregarding the short-wavelength modes we form a finite set of equations. In particular, assuming $|a_3|\ll|a_1|$ and choosing a_1 to be purely real (antisymmetric solution) we find

$$a_1=2\sqrt{\alpha[(2k_0)^2-1]}, \tag{3.2a}$$

$$a_2=-\frac{\alpha}{k_0}. \tag{3.2b}$$

If we extend our assumption to $|a_{n+2}|\ll|a_n|(n\geqslant 1)$ then a_n depends only on a_l, $l<n$, and a recursive formula for a_n can be easily found:

$$a_n=\frac{1}{2}\frac{1}{(nk_0)-(nk_0)^3}\sum_{l=1}^{n-1} a_l a_{n-l} \quad (n>2). \tag{3.2c}$$

A comparison with a numerical simulation (Fig. 2) confirms the validity of this construction.

The solution (3.2) is a fixed point in the phase space $\mathcal{U}$. The issue of stability of these solutions requires in principle the study of infinite-dimensional matrices. The reason is that the basic solution (3.1) contains infinitely many Fourier

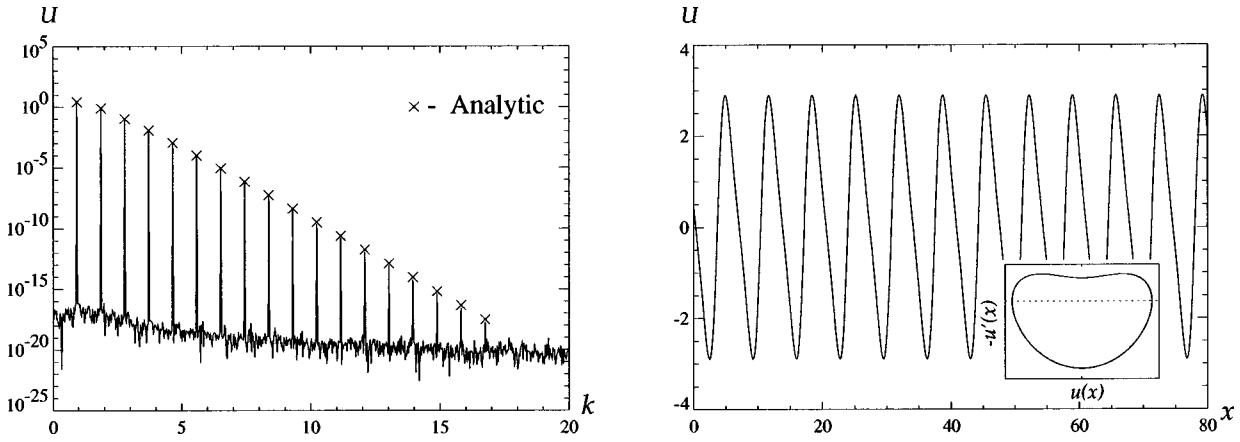

FIG. 2. Stationary cellular solution ($k_0=0.93$, $\alpha=0.7$). Left: comparison of the numerical and analytical spectrum $|U_h(k)|$. Right: $U_h(x)$. Inset: graph of $U_h(x)$ vs $-\partial_x U_h(x)$ (dashed line: $U'=0$).

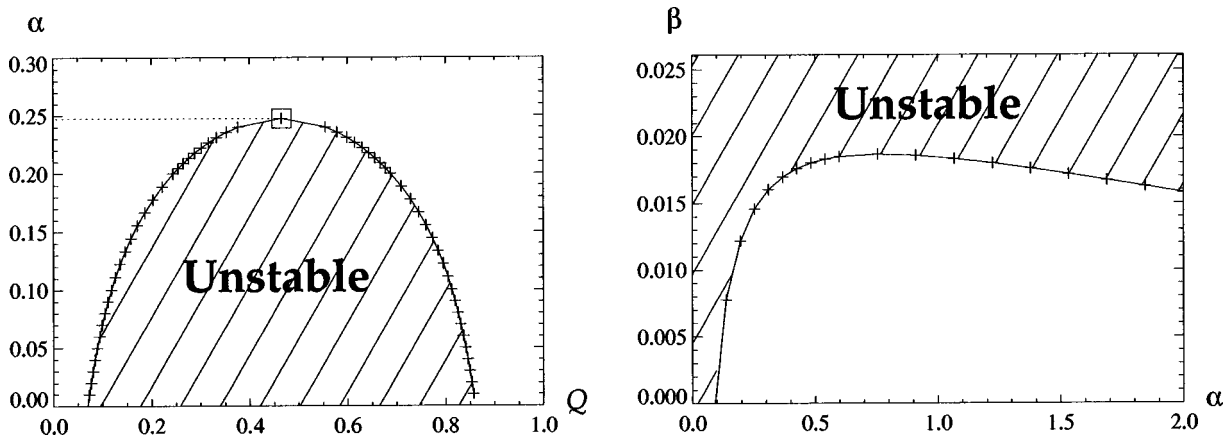

FIG. 3. Stability diagram for the time-independent cellular solution $U_h(x)$. Left: stability against perturbations at spatial frequency $Q \neq k_1$ ($k_0=0.93$). One eigenvalue crosses the imaginary axis on the line $\alpha_1(Q;k_0)$. The line has been calculated numerically using seven modes ($a_{-3},\ldots,a_3$). Right: stability against perturbations at $Q=k_1$ ($k_0=0.98$, $k_1=0.03$).

modes and the perturbations are coupled to all these modes. We show in Appendix A that the general form of a perturbation is

$$v(x,t)=e^{\lambda t}e^{iQx}\sum_n iv_n e^{ink_0x}, \tag{3.3}$$

where $Q\in[0,k_0)$. As before, due to the exponential decay of high-frequency modes, one can show (see Appendix A) that finite-dimensional approximations are sufficient for a proper stability analysis. The results are presented in Fig. 3. Stability can be discussed with respect to several parameters and the most important ones are Q and α. We conclude that (i) the system is stable against perturbations in the range $|Q|<1-k_0$ and (ii) the neutral curve [denoted below by $\alpha_1(Q;k_0)$] has an extremal value $\alpha_{\rm ext}$ and the system is stable against any perturbation for $\alpha>\alpha_{\rm ext}(k_0)$. The system becomes unstable again above a second branch: $\alpha>\alpha_2(Q;k_0)$ [see Eq. (A8)].

When $Q=k_1$ we add the contribution of $L(Q)=\beta$ to the stability matrix. Numerical calculations show that the eigenvalues are in the negative half plane, when $\alpha>\alpha_1(k_1,k_0)$ and $\beta<\beta_0(\alpha;k_1,k_0)$, as can be seen in the example in Fig. 3. We conclude that the fixed point $U_h(x)$ is stable when $\alpha>\alpha_{\rm ext}(k_0)$ and $\beta<\beta_0(\alpha;k_1,k_0)$.

B. The family of solutions of the first kind

The spectrum of the eigenvalues of the trivial solution $U(x)=0$ is equal to $L(k)$ [Eq. (2.10)]. When $\beta=0$, there is one unstable eigenvalue: $\lambda=L(k_0)=\alpha$. Therefore, the cellular solution $U_h(x)$ bifurcates from $U(x)=0$ at $\alpha=0$. In addition to the unstable eigenmode e^{ik_0x} there is a band of marginally stable eigenmodes e^{ikx}, $k\in(0,1)$. A k eigenmode can be nonlinearly unstable if $ks=k_0$, where s is an integer. Then, a periodic solution can bifurcate from $U(x)=0$. In this subsection we will see that the cellular solution $U_h(x)$ is just one member of a family of antisymmetric solutions of the form

$$U_I(x)=\sum_{n=-\infty}^{\infty} ib_{n/m}e^{i(n/s)\,k_0x},\quad b_{-n/m}=-b_{n/m}. \tag{3.4}$$

Every solution is characterized by a triplet of integers (m,s,p), where $m=\lfloor s/k_0\rfloor$ is the number of linearly nonstable modes in the range $k\in(0,1)$, s is the number of subharmonics in the range $k\in(0,k_0)$, and p is the periodicity of the solution defined as the number of zeros of its derivative $\partial_x U_I(x)$ in the interval $[x,x+s(\pi/k_0)]$. The triplet of integers corresponding to the solution $U_h(x)$ is $m=s=p=1$.

As an example we will study the case $m=3$. We start with $s=3$, i.e., $3/4<k_0<1$. The infinite set of equations is truncated beyond the first stable mode $b_{4/3}$. The justification of this truncation will be checked after the calculation of the coefficients of the first four modes. The equations for the four modes are

$$b_{1/3}b_{2/3}+b_{3/3}b_{2/3}+b_{3/3}b_{4/3}=0, \tag{3.5a}$$

$$\frac{1}{2}b_{1/3}^2-b_{3/3}b_{1/3}-b_{4/3}b_{2/3}=0, \tag{3.5b}$$

$$k_0b_{1/3}(b_{2/3}-b_{4/3})=\alpha b_{3/3}, \tag{3.5c}$$

$$\frac{4}{3}k_0(b_{1/3}b_{3/3}+\tfrac{1}{2}b_{2/3}^2)=L\left(\frac{4}{3}k_0\right)b_{4/3}. \tag{3.5d}$$

An additional assumption that will be used to solve Eq. (3.5b) is that $b_{4/3}b_{2/3}$ is much smaller than the other two terms in that equation. A solution of the set of equations is

$$b_{1/3}=\sqrt{\alpha\left[\left(\frac{4}{3}k_0\right)^2-1\right]-\left(\frac{\alpha}{8k_0}\right)^2}, \tag{3.6a}$$

$$b_{2/3}=\frac{\alpha}{8k_0}, \tag{3.6b}$$

$$b_{3/3}=\frac{1}{2}b_{1/3},\quad b_{4/3}=-3b_{2/3}. \tag{3.6c}$$

It is easy to see that this solution exists for $3/4<k_0<1$ and that the supplementary assumption holds when $\alpha\ll 18|L(\frac{4}{3}k_0)|$. At these values of α the amplitude of the higher modes ($n>4$) is indeed negligible compared to the

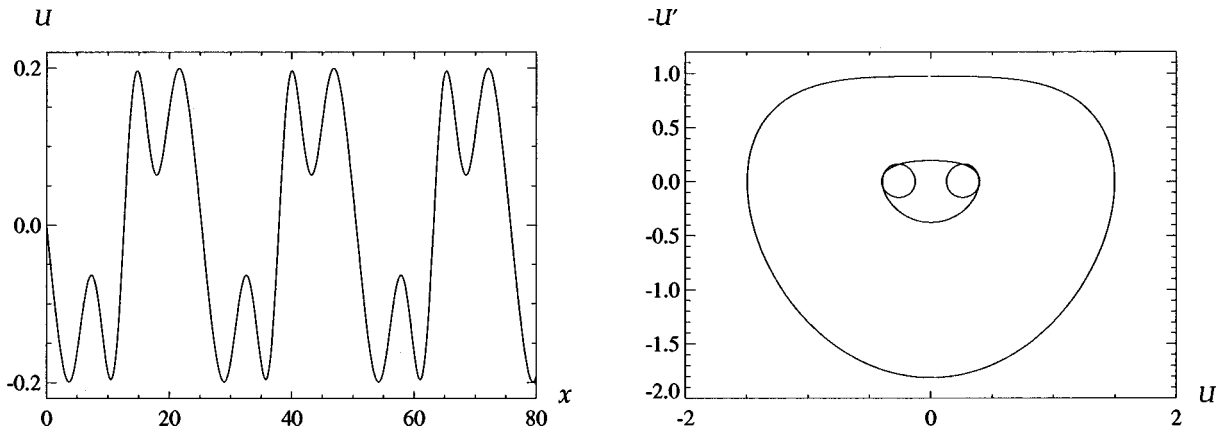

FIG. 4. Left: $U_I(x)$ at ($\alpha=0.21$, $k_0=0.93$) and ($s=m=3$). Right: two stationary solutions (at the same values of α and k_0): $U_h(x)$ (outer line) and the period-3 solution (3.6) (inner line).

four first modes. The full solution has been calculated numerically and it is seen in Fig. 4.

In general, when $s/(m+1)<k_0<s/m$ (s and m are integers and $s\leqslant m$), we look for a solution with s subharmonics. In the example $m=3$, there are solutions when $s=3$ and 1, but there is no solution when $s=2$.

Equation (3.5) has yet another $s=3$ solution, which is approximately

$$b_{1/3}=\frac{2}{3}\sqrt{\frac{\alpha^3}{k_0^2}\frac{1}{L\left(\frac{4}{3}k_0\right)}},\quad b_{2/3}=-\frac{\alpha}{k_0},$$

$$b_{3/3}=-b_{1/3},\quad b_{4/3}=-\frac{2}{3}\frac{\alpha^2}{k_0}\frac{1}{L\left(\frac{4}{3}k_0\right)}. \tag{3.7}$$

This approximation holds for $\alpha\ll L(\frac{4}{3}k_0)$. [When $L(\frac{4}{3}k_0)=0$ this solution coincides with the $m=4$, $s=3$ solution and for intermediate values of $L(\frac{4}{3}k_0)$ there is an intermediate solution that cannot be developed in powers of α.] The main difference between that solution and the previous one (3.6) is the periodicity p. The basic spatial frequency of solution (3.6) is k_0 and the periodicity is $p=3$ (see Fig. 4), while the principal spatial frequency of the new solution is $\frac{2}{3}k_0$, so its periodicity is $p=2$.

The $m=3$ solution (3.6) has a special symmetry in the limit $\alpha\to 0$: It is symmetric around the U axis ($U'=0$). In other words, $U(x)$ is an eigenfunction of the antisymmetric translation operator $\mathcal{R}_2[\ ]$ with an eigenvalue $\lambda=1$, where $\mathcal{R}_n[\ ]$ is defined by

$$\mathcal{R}_n[U(x)]=-U\left(x+\frac{2\pi}{k_0}\frac{s}{n}\right). \tag{3.8}$$

Before we give a general description of the family $U_I(x)$, we will briefly present a second example: $s=m=5$. (The full calculation of this example is given in Appendix B.) Four different solutions of this example are seen in Fig. 5. Two solutions are eigenfunctions of $\mathcal{R}_2[\ ]$. Two additional solutions $U(x)$ and $\overline{U}(x)$ can be paired such that $\mathcal{R}_2[U(x)]=\overline{U}(x)$. The periodicity of all these solutions is equal to $p=5$. In addition, there are other $m=5$ solutions with lower periodicity, $p=4$ and $p=3$ [see Eq. (B2b)]. It is very important for our understanding of the set of stationary solutions to observe that after appropriate scaling, the four

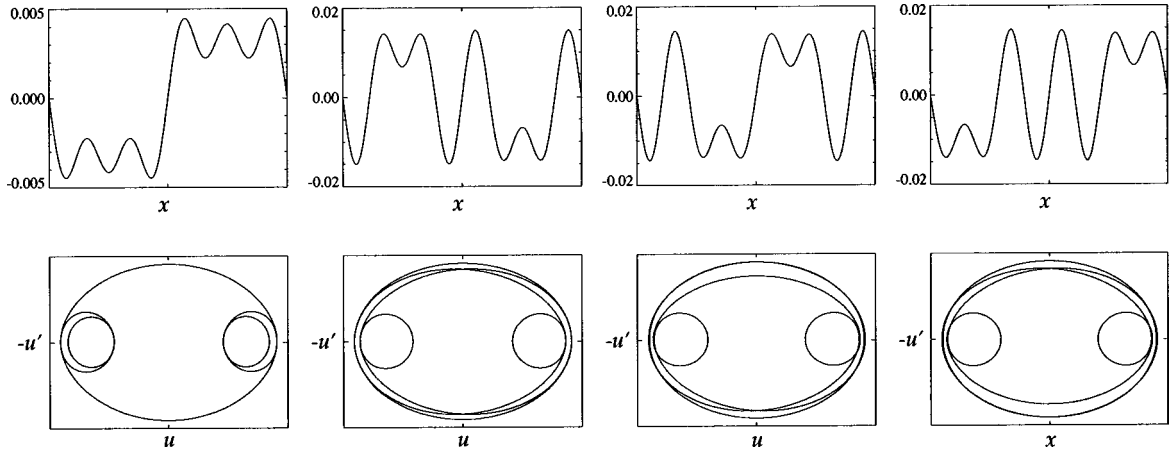

FIG. 5. Four solutions at ($\alpha=0.0001$, $k_0=0.93$) and ($s=m=5$). Upper: $U_I(x)$. Lower: the graphs at the (U,U') plane. The two leftmost figures are the solutions (B1); the two rightmost figures are the solutions (B7).

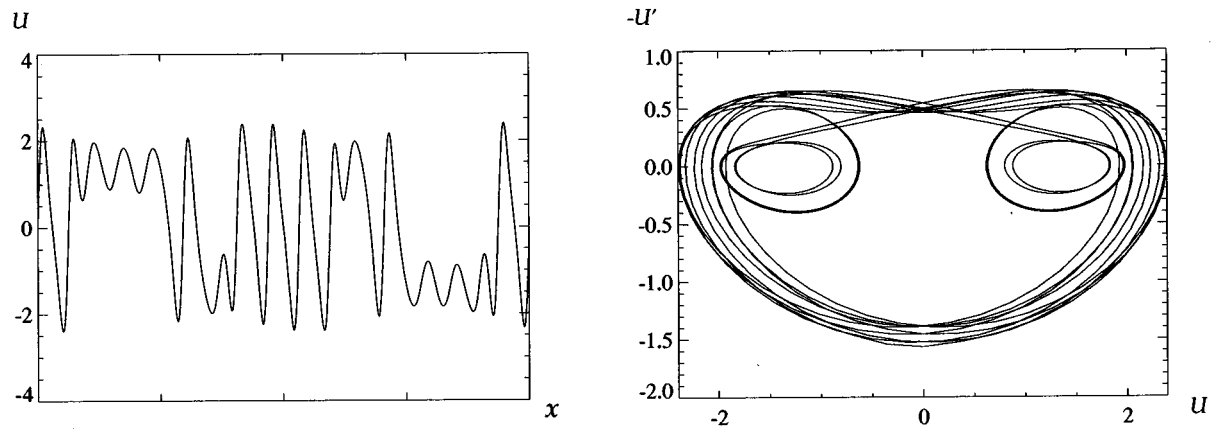

FIG. 6. Time-independent numerical solution of model equation. $\alpha=1.2$, $\beta=0.03$, $k_{\min}=0.053$, $k_1=2k_{\min}$, and $k_0=17k_{\min}$. Left: numerical solution $U(x)$. Right: curve of $U(x)$ vs $-\partial_x U(x)$.

solutions of Fig. 5 look very similar and, in particular, they ''start'' with essentially the same derivative at the beginning of the period.

C. The symbolic language and the topological entropy

The discussion of the qualitative nature of the solution is facilitated by the introduction of a symbolic language with a one-to-one correspondence between words in the language and solutions of the first kind. Since we deal with infinitely many degrees of freedom, the existence of such a language is not obvious. Its usefulness in classifying the solutions and ordering them in logical way is immense. In particular, the symbolic language will allow us to demonstrate the existence of a positive topological entropy of this family of solutions.

Looking at the graphs in the (U,U') plane (Figs. 4 and 5), we see that the orbits move periodically from the left half plane ($U<0$) to the right half plane ($U>0$). We denote by the symbols $\mathbf{L}_n$ ($\mathbf{R}_n$) a curved line segment in the left (right) half plane that crosses the $U'=0$ line $2n+1$ times. This means that there are n little loops before the orbit returns to the value $U=0$. Any stationary solution of the first type can be written as an expression in this language. The expression for the $U_h(x)$ solution is $(\mathbf{L}_0\mathbf{R}_0)^j$, where the integer j just counts the periodic repetitions (Fig. 2). In the usual way, we are interested in ''prime periods'' and hence only write $\mathbf{L}_0\mathbf{R}_0$ in this case. The expression for the antisymmetric solution with $m=3$ of Fig. 4 is $\mathbf{L}_1\mathbf{R}_1$. Similarly, the orbits of Fig. 5 are coded by $\mathbf{L}_2\mathbf{R}_2$, $\mathbf{L}_0\mathbf{R}_1\mathbf{L}_0\mathbf{R}_0\mathbf{L}_1\mathbf{R}_0$, $\mathbf{L}_0\mathbf{R}_0\mathbf{L}_1\mathbf{R}_1\mathbf{L}_0\mathbf{R}_0$, and $\mathbf{L}_1\mathbf{R}_0\mathbf{L}_0\mathbf{R}_0\mathbf{L}_0\mathbf{R}_1$. Because of translation invariance, the orbit described by $\mathbf{R}_1\mathbf{L}_1$ coincides with the one described by $\mathbf{L}_1\mathbf{R}_1$ (and similarly for any cyclic permutation of any code).

Our assertion is that, for sufficiently small $\alpha>0$, any expression of the form $\Pi_i\mathbf{L}_{n_i}\mathbf{R}_{n_i'}$ is realized as a stationary solution of the first kind. The periodicity of such a solution is

$$p=\sum_i (n_i+n_i'+1). \tag{3.9}$$

Clearly, for such a solution to exist, p must be smaller than or equal to m, the number of unstable modes. In Fig. 6 we show an example with $p=m=17$ and with the code $\mathbf{R}_0\mathbf{L}_0\mathbf{R}_3\mathbf{L}_0\mathbf{R}_0\mathbf{L}_1\mathbf{R}_0\mathbf{L}_0\mathbf{R}_0\mathbf{L}_0\mathbf{R}_0\mathbf{L}_0\mathbf{R}_1\mathbf{L}_0\mathbf{R}_1\mathbf{L}_3\mathbf{R}_0\mathbf{L}_0$.

Given the above rules, it is easy to construct the dictionary of all possible expressions with given periodicity. For example, the reader can verify that there are exactly four solutions with $p=5$, when $m=5$, namely, those shown in Figs. 2 and 4.

Having completed the examples, we turn to the evaluation of the number of available antisymmetric solutions of periodicity p. We will show that this number grows exponentially with p, in a scaling limit where α gets smaller as the required periods get larger. The exponent of this law of growth can be interpreted as the topological entropy that characterizes the spatial complexity of stationary solutions. These solutions form the backbone on which our understanding of spatiotemporal chaos is based.

We end this subsection by counting the number of solutions accommodated by the symbolic language. In the next subsection we will argue that they all exist if α is sufficiently small.

The number of antisymmetric expressions of periodicity p is equal to the total number of expressions of periodicity $p/2$:

$$N_p=\sum_{l=0}^{\lfloor p/3\rfloor}\sum_{i_1,\ldots,i_l=1}\binom{p-2\sum_{j=1}^{l} i_j}{l}\frac{1}{\overline{P}_{i_1,\ldots,i_l}}, \tag{3.10}$$

where $\overline{P}_{i_1,\ldots,i_l}$ is the normalized permutation number $\overline{P}_{i_1,\ldots,i_l}=P_{i_1,\ldots,i_l}/l!$ and $P_{i_1,\ldots,i_l}$ is the number of identical permutations of the set $\{i_1,\ldots,i_l\}$.

The maximum values of the i_j is determined by the condition $2\Sigma i_j\leqslant p-l$. N_p is bounded from above by the number of binary numbers of p digits and it is bounded from below by the number of binary numbers of $p/2$ digits. Therefore, N_p increases as $2^{\zeta_p p}$, where $1/2<\zeta_p<1$. Computation of the first elements of N_p shows that

$$N_p\simeq 0.464\times 2^{0.687p}. \tag{3.11}$$

In fact, it will be shown below that this family of solutions undergoes a rich multiplicity of cascades of bifurcations that give rise to a much larger number of solutions. The implication with regard to topological entropy will be discussed there.

D. Demonstration of the existence of N_p solutions of the first kind

We will examine, for small α, the general solution $U_I(x)$, characterized by m and s [see Eq. (3.4)]. We will argue that, generically, in a system of size $\mathfrak{L}=2\pi m$ there exist N_p [see Eq. (3.11)] stationary solutions of periodicity $p=m$.

As explained in Sec. III A, for analytic purposes it is sufficient to consider explicitly only the modes whose k lies in the interval [0,2]. We will argue that the amplitudes of the modes in this group do not scale uniformly with the bifurcation parameters. Defining a small parameter $\epsilon\sim\sqrt{\alpha}$ we will split the modes into one group whose amplitude scales like ϵ^{ν} and other groups whose amplitude is smaller, of order higher than ν. The appropriate value of ν will be determined later. To order $\epsilon^{2\nu}$ we work with the ansatz

$$b_{n/m}\simeq\begin{cases}\epsilon^{\nu}c_n, & 0<n\leqslant m\\ \epsilon^{\nu+1}d_n, & 0<n\leqslant m,\ \ c_n=0\\ \epsilon^{2\nu}d_n, & m<n\leqslant 2m.\end{cases}\tag{3.12}$$

When this ansatz is substituted in the model (2.2) and (2.10) one finds that the lowest-order equations depend only on the nonlinear operator. Therefore, these are m homogeneous equations of order $\epsilon^{2\nu}$ and they can be written as m quadratic forms

$$\boldsymbol{c}\boldsymbol{M}^l\boldsymbol{c}=\boldsymbol{0},\quad l=1,\ldots,m,\tag{3.13}$$

where $\boldsymbol{c}$ is an m component vector $(\boldsymbol{c})_n=c_n$ and the $\boldsymbol{M}^l$ are $m\times m$ matrices

$$M^l_{ij}=\frac{1}{2}(\delta_{i+j,l}-\delta_{i-j,l}-\delta_{-i+j,l})\quad(i,j,l=1,\ldots,m).\tag{3.14}$$

The set of equations (3.13) can be written as a single m component vector equation

$$\boldsymbol{\phi}(\boldsymbol{c})=\boldsymbol{0},\tag{3.15}$$

where $\phi_l(\boldsymbol{c})\equiv\boldsymbol{c}\boldsymbol{M}^l\boldsymbol{c}$.

In order to discuss the solutions of this equation, we define them as the limit, as $\mu\to 1$, of a family of solutions of a parametrized set of equations: We define $\boldsymbol{M}^l(\mu)$ such that $\boldsymbol{M}^l(1)=\boldsymbol{M}^l$:

$$M^l_{ij}(\mu)=M^l_{ij}+\frac{1}{2}(\mu-1)(\delta_{(m-i)+(m-j),l})\qquad(i,j,m-i,m-j,l=1,\ldots,m)\tag{3.16}$$

and the corresponding m quadratic forms

$$\phi_l(\boldsymbol{c};\mu)=\boldsymbol{c}\boldsymbol{M}^l(\mu)\boldsymbol{c}.\tag{3.17}$$

Clearly, Eq. (3.13) is now written $\boldsymbol{\phi}(\boldsymbol{c};1)=0$. The use of this parametrization is that for $\mu=0$, the solutions can be found explicitly. Indeed, the $\boldsymbol{M}^l(1)$ matrices are the Fourier space representation of the *nonaliased squaring operator on a grid* restricted to the subspace of antisymmetric functions. The normal *squaring operator on a grid* $U^2(x_j)$, restricted to the same subspace, is represented in Fourier space by the $\boldsymbol{M}^l(0)$ matrices. In other words, the lth mode of the discrete Fourier transform of $U^2(x_j)$ is equal to $\boldsymbol{c}\boldsymbol{M}^l(0)\boldsymbol{c}$, where $\boldsymbol{c}$ is the discrete Fourier transform of $U(x_j)$. Accordingly, the vector equation $\boldsymbol{\phi}(\boldsymbol{c};0)=\boldsymbol{0}$ can be written in real space as

$$\partial_x[U^2(x_j)]=0,\qquad x_j=\left(j+\frac{1}{2}\right)\frac{\pi}{k_0}\frac{s}{m}$$
$$U(x_{j+m})=-U(x_j),\quad -\infty<j<\infty,\tag{3.18}$$

where the operator ∂_x is defined in Fourier space by

$$\partial_x[U^2(x_j)]=\int dk\, ik\sum_h e^{ik(x_j-x_h)}U^2(x_h).\tag{3.19}$$

Equation (3.18) has 2^m solutions, which can be written as

$$U(x_j)=A[2y(x_j)-1],\tag{3.20}$$

where $y(x_j)$ is a binary digit, $y(x_j)\in\{0,1\}$, and A is an arbitrary amplitude. So a solution of Eq. (3.18) is represented by a string $\boldsymbol{y}$ of binary digits such that $(\boldsymbol{y})_j=y(x_j)$. The simplest example is $m=1$. Then $\boldsymbol{M}^1(0)=\boldsymbol{0}$ and the only nontrivial antisymmetric solution is $\boldsymbol{y}=\overline{01}$. This is the $U_h(x)$ solution.

In Appendix C we show that if there is a solution to the $m-1$ equations $\phi_l(\boldsymbol{c};\mu)=0$, $l<m$, at any μ, and $c_m\neq 0$, then we are guaranteed that this solution solves the m equations $\boldsymbol{\phi}(\boldsymbol{c};\mu)=0$ at $\mu=0$ and 1. (Notice that $c_m=0$ means that the periodicity p is smaller than m.) Accordingly, we define the set $\mathcal{P}(\mu)$ as the set of solutions of the $m-1$ equations $\phi_l(\boldsymbol{c};\mu)=0$, $l<m$. We already saw that at $\mu=0$, $\mathcal{P}(\mu)$ has 2^m solutions.

As μ is varied, the points of the set $\mathcal{P}(\mu)$ can be annihilated in pairs (see Appendix C). We want to know how many points survive when $\mu\to 1$. In Fig. 7 we show an example for $m=4$. The eight solutions of the three equations $\phi_l(\boldsymbol{c};\mu)=0$, $l=1,\ldots,3$, are

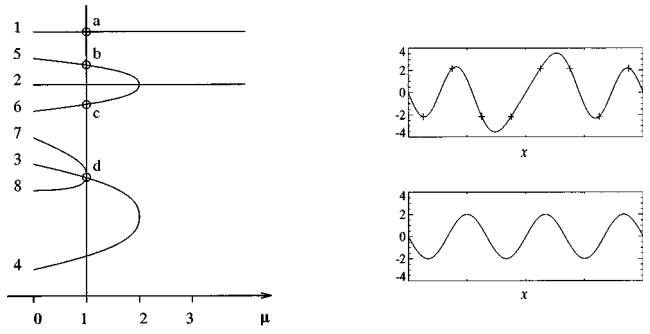

FIG. 7. Left: schematic bifurcation diagram of the set $\mathcal{P}(\mu)$ at $m=4$. Right: solution (7) at $\mu=0$ (upper) and $\mu=1$ (lower). The crosses denote the discrete solution (3.20): $\boldsymbol{y}=(0,1,0,0,1,1,0,1)$.

$$\boldsymbol{c}=\begin{cases}1,2: & (0,0,0,1),(0,1,0,0)\\ 3,4: & (1\mp\Omega,0,1,0)\\ 5,6: & \left(-\Omega-1,\pm\sqrt{2\dfrac{\Omega+1}{\Omega}},1,\pm\sqrt{2\Omega(\Omega+1)}\right)\\ 7,8: & \left(\Omega-1,\mp\sqrt{2\dfrac{\Omega-1}{\Omega}},1,\pm\sqrt{2\Omega(\Omega-1)}\right),\end{cases}\tag{3.21}$$

where $\Omega \equiv \sqrt{2-\mu}$. Solutions 2 and 4 fail to satisfy the mth equation $\phi_m(\mathbf{c};\mu)=0$ since $c_m=0$. Solutions 3, 7, and 8 change their real-space shape as μ increases from zero, as can be seen in Fig. 7, and they coincide at $\mu=1$. So only four different solutions survive at $\mu=1$, namely, those with the codes

$$a:\ (\mathbf{L}_0\mathbf{R}_0)^4, \quad b:\ \mathbf{R}_1\mathbf{L}_0\mathbf{R}_0\mathbf{L}_1,$$
$$c:\ \mathbf{L}_0\mathbf{R}_1\mathbf{L}_1\mathbf{R}_0, \quad d:\ (\mathbf{L}_0\mathbf{R}_0)^3. \tag{3.22}$$

Expressions $a-c$ are the only possible ones with periodicity $p=m=4$. The periodicity of solution d is $p=3$.

Since we lack an analytical description of the bifurcation scheme of the set $\mathcal{P}(\mu)$ for an arbitrary m, we will present instead a bifurcation scheme based on numerical experiments of examples up to $m=30$. At $\mu=0$ we assign to every solution $\mathbf{c}$ an expression of the form $\Pi_i \mathbf{L}_{n_i}\mathbf{R}_{n_i'}$, which characterizes its real-space discrete Fourier transform $U(x_j)$. To each sequence of zeros and ones, as defined by Eq. (3.20), $0^{2n_1+1}1^{2n_1'+1}\cdots 0^{2n_l+1}1^{2n_l'+1}$, we associate the product above. Note that the n_i and n_i' are nonnegative half integers here.

As $\mu\to 1$, the numerics show that only the solutions with integer n_i, n_i' survive. Indeed, we observe that those factors with half integer n are modified as μ is changed and reach finally the integer part of n, as $\mu\to 1$. Accordingly, the periodicity p of these solutions is lowered at $\mu=1$, as illustrated by solution 7 of the example above. Those solutions that do not contain any half integer n_i conserve their expression when μ is increased. Their periodicity is conserved, and since $p=m$, c_m is nonzero so these solutions solve Eq. (3.15). The numerical experiments indicate that they all exist at $\mu=1$.

If we know that a solution to Eq. (3.13) exists, we can find it using analytical or numerical methods. Two more steps should be taken in order to fix ϵ, the amplitude of the solution. First, we write all the $O(\epsilon^{2\nu})$ equations for the modes d_n where $m<n\leqslant 2m$. These equations are trivially solved by

$$d_n=\frac{1}{L_n}\sum_{j=1}^{m} c_j c_{n-j}, \quad m<n\leqslant 2m, \tag{3.23}$$

where $L_n=L[n(k_0/s)]/[n(k_0/s)]$. The next step is to find the amplitudes d_n where $n\leqslant m$. The c_n dictate the symmetries of a solution. A simple calculation shows that when a solution is an eigenfunction of an operator $\mathcal{R}_n$ [see Eq. (3.8)] there are $\Gamma=\lfloor m/n+\frac{1}{2}\rfloor$ such d_n (i.e., modes where $c_n=0$) and Γ equations of order $\epsilon^{2\nu+1}$,

$$\sum_{j=1}^{n-1} c_j d_{n-j} - \sum_{j=n+1}^{m} c_j d_{j-n} - \sum_{j=1}^{m} c_j d_{n+j} = 0. \tag{3.24a}$$

There is yet another equation of order $\epsilon^{2\nu+1}$ for the c_s mode:

$$\epsilon^{2\nu+1}\left(\sum_{j=1}^{s-1} c_j d_{s-j} - \sum_{j=s+1}^{m} c_j d_{j-s} - \sum_{j=1}^{m} c_j d_{s+j}\right) = \frac{\alpha}{k_0} b_s. \tag{3.24b}$$

Equation (3.24b) determines the value of ν according to the value of c_s:

$$\nu=\begin{cases} 1, & c_s\neq 0 \\ 2, & c_s=0. \end{cases} \tag{3.25}$$

For example, in the $m=3$ case that we studied before, there was one $\nu=1$ solution [Eq. (3.6)] and one $\nu=2$ solution [Eq. (3.7)]. When $c_s\neq 0$, we substitute the solutions (3.23) in Eqs. (3.24) and then they can be written in a matrix form

$$\boldsymbol{A}\boldsymbol{d}=\boldsymbol{\alpha}, \tag{3.26}$$

where $\boldsymbol{A}$ is a $(\Gamma+1)\times(\Gamma+1)$ matrix (c_n and L_n), $\boldsymbol{d}$ is the vector of the $(\Gamma+1)$ unknowns $\boldsymbol{d}=\epsilon^2(d_{n_1},\ldots,d_{n_\Gamma},1)$, and $\boldsymbol{\alpha}$ is a given vector equal to $[0,\ldots,0,0,(\alpha/k_0)c_s]$. The solution vector $\boldsymbol{d}=\boldsymbol{A}^{-1}\boldsymbol{\alpha}$ completes the calculation of the $2m$ coefficients $b_{1/m},\ldots,b_2$. When $c_s=0$, there is no generic solution unless $\Gamma=m-1$. In that case Eq. (3.24b) can be written in a matrix form

$$\boldsymbol{A}(c_s,\alpha)\boldsymbol{d}=0, \tag{3.27}$$

where $\boldsymbol{A}(c_s,\alpha)$ is a $\Gamma\times\Gamma$ matrix and $\boldsymbol{d}$ is a vector of Γ unknowns: $\boldsymbol{d}=\epsilon^2(d_{n_1},\ldots,d_{n_\Gamma})$. The eigenvalue of $\boldsymbol{A}$ determines $c_s(\alpha)$ and the eigenvector determines $\boldsymbol{d}$, up to its amplitude. The $\mathcal{O}(\epsilon^6)$ quadratic equation for the nonzero c_n mode determines the amplitude of $\boldsymbol{d}$ and completes the computation.

In summary, in the present subsection we studied the U_I family of solutions in the limit of small α. We saw that the properties of these solutions are determined by the nonlinear operator alone and therefore the generic solutions scale like $\sqrt{\alpha}$. [The nongeneric cases are those solutions where $c_s=0$ ($s=k_0\mathfrak{L}/2\pi$).] The spectrum of these solutions fills the range of k modes from zero to one. We found that, generically, in a system of size $\mathfrak{L}=2\pi m$ there are $N_p=2^{\zeta_p m}$ stationary solutions of periodicity $p=m$. So the entropy per unit length of this system is positive.

E. Bifurcations of solutions of the first kind

In this section we study the period n-tupling bifurcations of the solutions of the first kind. We examine in detail the bifurcations of the cellular solution $U_h(x)$ [Eq. (3.1)] and its transition to spatial chaos. Then we will argue that all the solutions of the first kind go through a multiplicity of cascades of period-n-tupling bifurcations.

1. Spatial period-doubling bifurcations of the cellular solution $U_h(x)$

In the beginning of this section we saw that the stability of the harmonic solution $U_h(x)$ changes at the critical line $\alpha_1(Q;k_0)$, as the largest eigenvalue of the stability matrix crosses the imaginary axis. When this happens a bifurcation occurs and a new branch of solutions can emerge from the bifurcation point. Due to the quadratic nonlinearity, the perturbed harmonic solution $U_h(x)+e^{\lambda t}\Sigma_n(v_n e^{i(Q+nk_0)x}+\text{c.c.})$ can saturate if $Q=\frac{1}{2}k_0$. In the current subsection, the antisymmetric period-2 solution

$$U_h^{(2)}(x)=\sum_{n=-\infty}^{\infty} ib_{n/2}e^{i(n/2)k_0x}, \quad b_{-n/2}=-b_{n/2}, \tag{3.28}$$

will be investigated. The equations of the integer modes (n even),

$$\sum_{l=-\infty}^{\infty} b_{l+1/2}b_{n-1/2-l}+\sum_{l=-\infty}^{\infty} b_l b_{n-l}=\frac{2}{k_0}L(nk_0)b_n, \tag{3.29a}$$

together with the equations of the half integer modes (n odd),

$$\sum_{l=-\infty}^{\infty} b_{l+1/2}b_{n-l}=\frac{1}{k_0}L[(n+1/2)k_0]b_{n+1/2}, \tag{3.29b}$$

suggest that above the bifurcation point the solution can be approximated by

$$b_{n/2}\simeq\begin{cases} a_{n/2}+\epsilon^2 c_{n/2}, & n \text{ even} \\ \epsilon c_{n/2}, & n \text{ odd}, \end{cases} \tag{3.30}$$

where the a_m are the coefficients of the harmonic solution (3.1) and ϵ is a small parameter. When we substitute Eq. (3.30) into Eqs. (3.29) and expand them in ϵ, we find equations for any order. The order-one equations are trivially fulfilled by the a_m. The half-integer mode equations are of order ϵ and they are identical to Eq. (A3) with $\lambda=0$, where the $v_{(n-1)/2}$ are replaced by $c_{n/2}$. Hence the period-2 solution $U_h^{(2)}(x)$ bifurcates from the harmonic solution $U_h(x)$ at $\alpha_c^{(2)}=\alpha_1(k_0/2;k_0)=\alpha_{\rm ext}(k_0)$. The second-order equation for the b_1 mode reads

$$(\mathcal{A}+\mathcal{B})\epsilon^2=\frac{a_1}{k_0}(\alpha-\alpha_{\rm ext}), \tag{3.31}$$

where

$$\mathcal{A}=\frac{1}{2}\sum_{n=-\infty}^{\infty} c_{n+1/2}c_{1/2-n}, \quad \mathcal{B}=\sum_{n=-\infty}^{\infty} c_n a_{1-n}-c_1\frac{\alpha_{\rm ext}}{k_0}. \tag{3.32}$$

From Eqs. (3.30) and (3.31) we find the scaling behavior of the $b_{n/2}$:

$$b_{n/2}(\alpha)=\begin{cases} b_{n/2}(\alpha_c)+(\alpha-\alpha_{\rm ext})\hat{c}_{n/2}, & n \text{ even} \\ (\alpha-\alpha_{\rm ext})^{0.5}\hat{c}_{n/2}, & n \text{ odd}. \end{cases} \tag{3.33}$$

The numerical solution of the set of nonlinear equations for the first 13 modes ($b_{-6/2},\ldots,b_{6/2}$) confirms this result. A translation of $U_h^{(2)}(x)$ by $2\pi/k_0$ gives a second antisymmetric period-doubling solution with coefficients $\tilde{b}_{n/2}=(-1)^n b_{n/2}$.

The stability of the period-2 solution $U_h^{(2)}(x)$ can be tested by the method that has been used to calculate the stability of the solution U_h. We show in appendix A that the global stability picture of $U_h^{(2)}$ is similar to that of U_h. In the (α,Q) parameter space there is a neutral curve $\alpha_1^{(2)}(Q;k_0)$, where the upper eigenvalue crosses the imaginary axis. However, in contrast to U_h (Fig. 3), the unstable region is *above* the neutral curve and therefore $U_h^{(2)}$ is unstable at any value of α.

$\alpha_1^{(2)}(Q;k_0)$, like $\alpha_1(Q;k_0)$, has an extremum at $\alpha_{\rm ext}^{(2)}=\alpha_1^{(2)}(k_0/4;k_0)$. At that point, a secondary period-doubling bifurcation to a new solution $U_h^{(2^2)}(x)=\Sigma_n ib_{n/4}e^{i(n/4)k_0x}$ takes place. We show in Appendix A that beyond the bifurcation point there is one positive eigenvalue and the *second* eigenvalue will cross the imaginary axis on the neutral curve $\alpha_1^{(2^2)}(Q;k_0)$.

The scaling of the coefficient $b_{n/4}$ beyond the bifurcation point is similar to the first period-doubling bifurcation. It is easy to see that similarly to $U_h^{(2)}(x)$, the coefficients of $U_h^{(2^2)}(x)$ scale with two different scaling exponents: the odd modes scale like $(\alpha-\alpha_c)^{0.5}$ and the even modes scale like $\alpha-\alpha_c$.

This period-doubling process repeats itself again and again and we have an infinite cascade of spatial period-doubling bifurcations at the points $\alpha_{\rm ext}^{(2^n)}=\alpha_1^{(2^n)}(k_0/2^n;k_0)$. Above any bifurcation point the stability matrix has positive eigenvalues and hence the solutions $U_h^{(2^n)}$ are unstable, but one eigenvalue changes its sign on the neutral curve $\alpha_1^{(2^{n+1})}(Q;k_0)$. The series of bifurcation points $\alpha_{\rm ext}^{(2^n)}$ converges geometrically to $\alpha_{\rm ext}^{(2^\infty)}$:

$$\alpha_{\rm ext}^{(2^\infty)}-\alpha_{\rm ext}^{(2^n)}\sim\delta_2^{-n}. \tag{3.34}$$

We followed the first five bifurcations (at $k_0=0.93$, using 241 modes) and found the scaling to be

$$\delta_2\equiv\lim_{n\to\infty}\frac{\alpha_{\rm ext}^{(2^{n-1})}-\alpha_{\rm ext}^{(2^n)}}{\alpha_{\rm ext}^{(2^n)}-\alpha_{\rm ext}^{(2^{n+1})}}=10\pm1. \tag{3.35}$$

A system of infinite extent shows spatial chaotic behavior beyond the accumulation point. Just above $\alpha_{\rm ext}^{(2^\infty)}$, $U(x)$ appears as a noisy 2^n periodic function, i.e., the spatial spectrum becomes continuous around the apices of the nth level. When α is further increased the spatial spectrum loses its organized structure. Although a finite system cannot show spatial chaos, still we can say that it is disordered or close to a chaotic solution if it goes to a spatially chaotic solution in the limit $k_{min}\to0$.

2. Spatial period-n-tupling bifurcations of the cellular solution $U_h(x)$

The period-doubling bifurcation is only one example of a wider family of n-tupling bifurcations [12]. A perturbation with a rational normalized wave number $Q/k_0=r/s$, where r and s are integers, can be nonlinearly saturated together with the $s-1$ other modes

$$Q=\frac{n}{s}k_0, \quad n=1,\ldots,s-1, \tag{3.36}$$

to one period-s solution

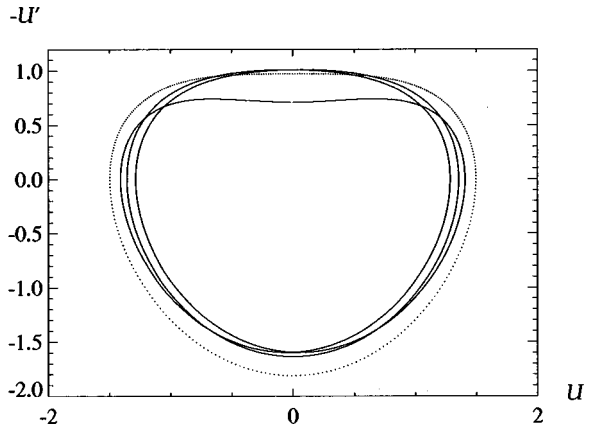

FIG. 8. Two stationary solutions at ($\alpha=0.21$, $k_0=0.93$): $U_h^{(3)}(x)$ (solid line) and $U_h(x)$ (dotted line).

$$U_h^{(s)}(x)=\sum_{n=-\infty}^{\infty} ib_{n/s}e^{i(n/s)k_0x}, \quad b_{-n/s}=-b_{n/s}. \tag{3.37}$$

The simplest example is $s=3$. We show in Fig. 8 the graph of a period-3 solution $U_h^{(3)}(x)$ in the (U,U') plane. Note the small modulations around the period-1 solution $U_h(x)$. The solution found here should not be confused with the other period-3 solution $U_I(x)$. If we compare the graphs of the two solutions in the (U,U') plane (Figs. 4 and 8), we see that the two solutions are of a different nature.

The period-3 solution bifurcates from $U_h(x)$ on the neutral curve $\alpha_1(Q;k_0)$ at the point

$$Q=k_0/3,$$

$$\alpha_c^{(3)}=\alpha_1(k_0/3;k_0).$$

We saw in Sec. III A that $\alpha_1(Q/3;k_0)=0$ when $Q<(1-k_0)$ and therefore $U_h^{(3)}(x)$ exists only if $k_0>s/(s+1)=3/4$. Numerical study of $U_h^{(3)}(x)$ shows that it exists at $k_0>0.769$. The equations of noninteger modes, for example,

$$2\sum_{n=-\infty}^{\infty} b_{n+1/3}b_{l-n}+\sum_{l=-\infty}^{\infty} b_{n+2/3}b_{l-1/3-n} =\frac{2}{k_0}L[(l+1/3)k_0]b_{l+1/3}, \tag{3.38}$$

together with the equations of the integer modes, suggest that near the bifurcation point the solution scales like

$$b_{n/3}\simeq\begin{cases} a_{n/3}+\epsilon c_{n/3}, & (n \mod 3)=0 \\ \epsilon c_{n/3} & \text{otherwise,}\end{cases} \tag{3.39}$$

where the a_n are the coefficients of $U_h(x)$ and ϵ is a small parameter. Notice that this scaling is different from the scaling near the period-doubling bifurcation [Eq. (3.30)]. The equation for the b_1 mode reads

$$\mathcal{A}\epsilon^2+\mathcal{B}\epsilon=\frac{a_1}{k_0}(\alpha-\alpha_c^{(3)}), \tag{3.40}$$

where similarly to Eq. (3.32)

$$\mathcal{A}=\sum_{n=-\infty}^{\infty} c_{n+1/3}c_{2/3-n}, \quad \mathcal{B}=\sum_{n=-\infty}^{\infty} a_nc_{1-n}-c_1\frac{\alpha_c^{(3)}}{k_0}. \tag{3.41}$$

Accordingly, the bifurcation is *transcritical*:

$$b_{n/3}(\alpha)=b_{n/3}(\alpha_0)\pm\hat{c}_{n/3}(\alpha-\alpha_0)^{0.5}, \tag{3.42}$$

where

$$\alpha_0=\alpha_c-\frac{1}{4}\frac{k_0}{a_1}\frac{\mathcal{B}^2}{\mathcal{A}}. \tag{3.43}$$

In Appendix A we show that the solution $U_h^{(3)}(x)$ has zero eigenvalues at α_c and α_0, as in transcritical bifurcations of low-dimensional dynamical systems (ordinary differential equations). However, unlike low-dimensional dynamical systems, $U_h^{(3)}(x)$ is unstable at any value of the control parameter α.

A richer behavior is found when $s>3$. The neutral curve $\alpha_1(Q;k_0)$ is nonzero in the band $1-k_0<Q<2k_0-1$ (see Fig. 3) and therefore periodic solutions can bifurcate for any $s<k_0/(1-k_0)$. A real perturbation contains two basic modes Q and k_0-Q (and all their harmonics). Accordingly, $\lfloor s/2\rfloor$ different perturbations build one period-s function (3.37) and they can be combined in several ways to build different period-s solutions. For any s there are $\lfloor s/2\rfloor$ different bifurcation points on the neutral curve:

$$\alpha_c^{(s;r)}=\alpha_1\left(\frac{r}{s}k_0;k_0\right), \quad r=1,\ldots,\lfloor s/2\rfloor. \tag{3.44}$$

As an example we will briefly examine the case $s=5$ where there are $\lfloor s/2\rfloor=2$ bifurcations on the neutral curve. Near $\alpha_c^{(5;r)}$ the leading order of the marginal mode is ϵ, while the other mode scales like ϵ^2:

$$b_{n/5}\simeq\begin{cases} a_{n/5}+\epsilon^2d_{n/5}, & n \mod 5=0 \\ \epsilon c_{n/5}\delta_{r,\rho}+\epsilon^2d_{n/5}, & n \mod 5=\rho,5-\rho \quad (\rho=1,2;r=1,2).\end{cases} \tag{3.45}$$

Accordingly, the bifurcation equation reads

$$\sum_{m=2}^{4} \mathcal{A}_m^{(5;r)} \epsilon^m = \frac{a_1}{k_0}(\alpha - \alpha_c^{(5;r)}), \tag{3.46}$$

where the factors $\mathcal{A}_m$ are defined similarly to Eq. (3.41). The number of turning points on the bifurcation curve $\epsilon^{(5;r)}(\alpha)$ could be one or three, depending on the signs of the factors. We found numerically, at $k_0 = 0.93$, that $\epsilon^{(5;1)}$ has three turning points, while $\epsilon^{(5;2)}(\alpha)$ has only a minimum point at $\alpha = \alpha_c^{(5;1)}$ (saddle-node bifurcation). Notice that translation of any of the period-5 solutions by $5\pi/k_0$ gives another antisymmetric solution with coefficients $\tilde{b}_{n/5} = (-1)^n b_{n/5}$.

We saw that in addition to the period-doubling bifurcation there is a finite set of possible bifurcations on the neutral curve $\alpha_1(Q,k_0)$ at any periodicity s such that $s = Q/k_0 = 2,3,\ldots,\lfloor k_0/(1-k_0) \rfloor$. The bifurcation curve has one to $\lfloor s/2 \rfloor$ turning points. The period-s solutions $U_h^{(s)}(x)$ are small modulations around $U_h(x)$, as can be seen in the example in Fig. 8. Any of the solutions $U_h^{(s)}(x)$ has its own neutral curve where one eigenvalue crosses the imaginary axis (notice that the highest eigenvalue is always positive, i.e., these solutions are unstable). On that line a secondary bifurcation, with a different s, can take place, yielding inductively a hierarchical structure of bifurcations [12]. Accordingly, we can find infinitely many different routes to spatial chaos through an infinite series of bifurcations $\mathbf{\Sigma} = (s_1 s_2 \ldots)$, where $\mathbf{\Sigma} = 2^\infty$ is the period-doubling route.

Finally, we note that in addition to the neutral line bifurcations, when $s \geqslant 5$ there are other s periodic solutions, close to $U_h(x)$, that arise at finite α. Accordingly, these solutions are finite at the bifurcation point. For example, when $s = 5$ there is one solution, with two branches, that bifurcates at $\alpha_c^{(5;1)} < \alpha < \alpha_c^{(5;2)}$. At higher values of s there are more such solutions. A similar family of stationary period-n solutions has been found numerically for the Kuramoto-Sivashinsky equation [13].

F. Summary

The upshot of this section is that the family of stationary solutions of the first kind is very rich indeed even in our simplified model. We showed that we can propose a symbolic language that describes the organization and counting of the basic periodic solutions in this family. On top of these basic solutions there is a complex array of n-tupling bifurcations that results in an even richer spatial complexity in the topological sense. Although we considered in detail the bifurcation scheme of the cellular solution $U_h(x)$ only, it can be shown that all other members of the U_I family that can be written as $(\Pi_i \mathbf{L}_{n_i} \mathbf{R}_{n_i'})^\infty$, go through similar bifurcations as α is raised, until they become spatially chaotic.

Notice that beyond any bifurcation point the new period-n solutions coexist with the old ones. Solutions do not disappear, but they usually exchange their stability with the new period-n solutions. Accordingly, the spatial topological entropy that we estimated before is just a lower bound to the rate of increase of allowed solutions. This explains in part the unmanageable complexity of stationary solutions available for the case of the Kuramoto-Sivashinsky equation.

IV. A FAMILY OF SOLUTIONS OF THE SECOND KIND

In this section we turn to the discussion of a second family of solutions that are qualitatively different from those labeled as ''First Kind.'' The main characteristic of solutions of the second kind is that they display a scale that is of the order of the size of the system. In that scale these solutions are related to typical phenomena that occur in experimental systems. It has been often observed in the transition to chaos in experimental systems that there exists a *mean flow* (or *drift flow*), which is a flow whose length scale is large compared to the wavelength of the cellular state (e.g., convection rolls) [14–17]. Numerical experiments of the model (2.2) and (2.10) exhibit stationary and time-dependent solutions whose typical length scale is of the order of the system size. Using the control parameter β we can control the time dependence of this solution. When β is larger than a critical value β_c, the large-scale solutions are stable. When β is lowered, these solutions pass through a series of Hopf bifurcations. The first transition is to a temporally periodic solution and then the solutions become quasiperiodic and finally temporally chaotic. This family of solutions is denoted $U_{II}(x,t)$.

In Sec. III we saw that when a U_I solution is substituted into the model equation, the lowest-order terms are determined by the nonlinear operator alone. This implies that the amplitude of the solution is proportional to the square root of the control parameter. In addition, the set of solutions is invariant, in the lowest order, under inversion $U_I(x) \rightarrow -U_I(x)$. In contrast, we will see that for the U_{II} family the linear and nonlinear terms are of the same order and therefore the solutions are proportional to the control parameter and are not invariant under inversion.

A. Stationary solutions

Our discussion is based on the observation that we can find an exact stationary long-wavelength solution to the model equation (2.2) when the linear operator has only one unstable mode and no stable modes, i.e., if $L(k)$ is of the form

$$L(k) = \beta \delta(|k| - k_1), \quad \beta > 0. \tag{4.1}$$

Indeed, we shall check that the time-independent function U_c is a solution of Eq. (2.2) with L as in Eq. (4.1):

$$U_c(x) = A \frac{\beta}{k_1} \sin\left(\frac{k_1}{2}x\right) w\left(\frac{k_1}{2}x\right), \tag{4.2}$$

where $w(\theta)$ is the Walsh cal$[1,(\theta - \pi/2]$ function

$$w(\theta) \equiv \begin{cases} 1 & \text{if } \dfrac{\pi}{2} \leqslant \theta < \dfrac{3\pi}{2} \\ -1 & \text{otherwise.} \end{cases} \tag{4.3}$$

Substitution into Eq. (2.3) gives

$$\mathcal{N}[U_c(x)] = \left(\frac{A\beta}{2k_1}\right)^2 k_1 \sin(k_1 x). \tag{4.4}$$

The Fourier transform of $U_c(x)$ is

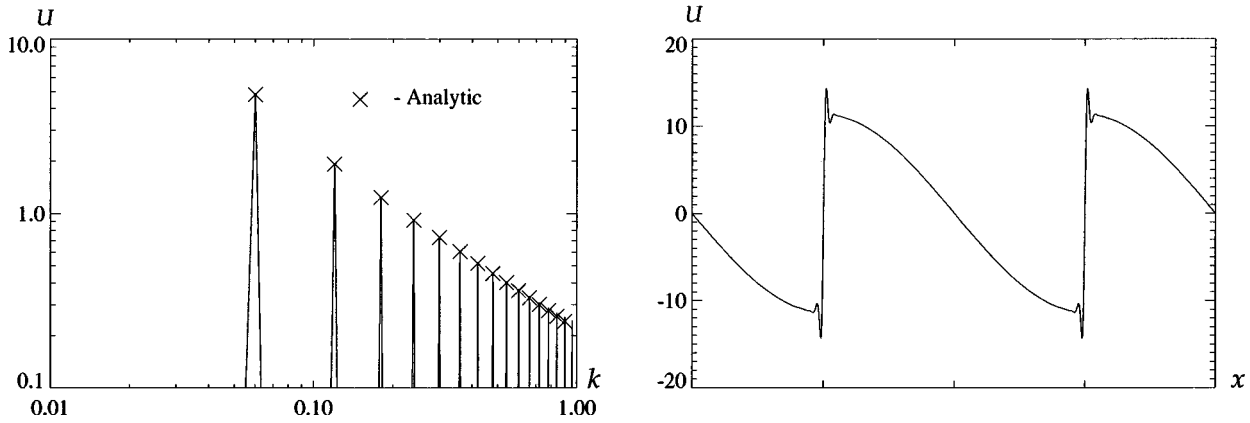

FIG. 9. Time-independent solution of the model (2.2) and (2.10). $\beta=0.2$, $k_1=0.06$, $k_0=0.93$, and $\alpha=1.2$. Left: comparison of numerical and analytical spectrum $|U_c(k)|$ at $k<1$. Right: real-space numerical solution $U_c(x)$. Inset: curve of $U_c(x)$ vs $-\partial_x U_c(x)$. The large ''excursion'' is due to the sharp jumps, while the flat connection is due to the monotonically decreasing part of the solution. The reader can compare it to the $y^{(-2)}$ orbit in Ref. [20].

$$U_c(x)=\frac{\beta}{k_1}\sum_{n=1}^{\infty}2u_n\sin(nk_1x), \tag{4.5a}$$

$$u_n\equiv\frac{A}{\pi}(-1)^n\left(\frac{1}{2n-1}+\frac{1}{2n+1}\right). \tag{4.5b}$$

If we choose the amplitude of $U_c(x)$ as

$$A=\pi a,\quad a=\frac{32}{3\pi^2}\simeq 1.08, \tag{4.6}$$

then, indeed, U_c solves Eq. (2.2) with the linear operator (4.1). In Fig. 9 we compare the solution $U_c(x)$ and the numerical solution of the model equation with the full linear operator (2.10). It is manifest that they are very close, and this is the basis of the following discussion.

When k_0 is sufficiently incommensurate with k_1, the linear operator (2.10) deviates from Eq. (4.1) only at $k>1$, so $U_c(x)$ is close to the exact time-independent solution of Eq. (2.10) at $k<1$, as we can see in the figure. When k_0/k_1 is an integer there are small deviations from $U_c(x)$ at $k\sim k_0$. In the remainder of this section we will use the solution $U_c(x)$ as an approximation to the exact solution of the model (2.2) and (2.10).

The ansatz for $U_c(x)$ [Eq. (4.2)] contains sharp discontinuities at $x_0=(1/k_1)(n+\frac{1}{2})\pi$. Accordingly, its spectrum decays like $1/k^2$. Of course, due to the dissipative modes in the linear operator, high spatial modes will be exponentially damped [18] and the discontinuities will broaden. We denote the width of the ''discontinuities'' by l_0. Since $|U_c(k)|^2$ starts to decay like $1/k^2$ at spatial modes smaller than $k\sim 1/l_0>1$ and exponentially above it, l_0 is a ''Kolmogorov scale.'' Hence a better approximation for $U_c(x)$ near the discontinuities is

$$U_c(x)=\frac{2}{\pi}\,\mathrm{Si}\left(\frac{x-x_0}{l_0}\right),\quad |x-x_0|\ll\frac{\pi}{2}\frac{1}{k_1}, \tag{4.7}$$

where $\mathrm{Si}(z)$ is the sine integral function $\mathrm{Si}(z)=\int_0^z[\sin(t)/t]dt-\pi/2$. The limit $l_0\to 0$ is the jump limit, while for finite l_0 it decays like $1/k^2$ for spatial modes smaller than $1/l_0$ and is zero for higher modes. Similar oscillatory shock solutions have been found in numerical studies of the Kuramoto-Sivashinsky equation with homogeneous Neumann boundary conditions [19,20].

Define the field $h(x,t)\equiv\frac{1}{2}\int_0^x dy\,U(y,t)$. By integrating the solution (4.2) one obtains

$$h(x)\propto\left|\cos\left(\frac{k_1}{2}x\right)\right|. \tag{4.8}$$

Notice that other Galilean invariant equations such as Burger's equation and Sivashinsky's equation have similar solutions [21]:

$$h(x)\propto\ln[|\cos(x)|],\quad \text{(Burger's equation)},$$

$$h(x)\propto\ln[|a-\cos(x)|]\quad \text{(Sivashinsky's equation)}. \tag{4.9}$$

For a given set of parameters $(\alpha,\beta,k_0\ldots)$ one can find a second long-wavelength stationary solution. We will show that a solution with very complex spatial spectrum (see the inset in Fig. 10) can be analyzed analytically when one chooses the appropriate variables to describe it. We look for a solution of the form

$$U_d(x)=\frac{\beta}{k_1}\sin\left(\frac{k_1}{2}x\right)w\left(\frac{k_1}{2}x;\vartheta\right)z(x), \tag{4.10}$$

where $w(\theta;\vartheta)$ is the symmetric rectangular wave

$$w(\theta;\vartheta)=\begin{cases}1 & \text{if } \dfrac{\pi}{2}-\vartheta\leqslant\theta<\dfrac{3\pi}{2}+\vartheta\\ -1 & \text{otherwise}\end{cases} \tag{4.11}$$

and $z(x)$ is an unknown function of x. The Fourier component of the nonlinear term $\mathcal{N}[U_d(x,t)]$ at spatial frequency k is

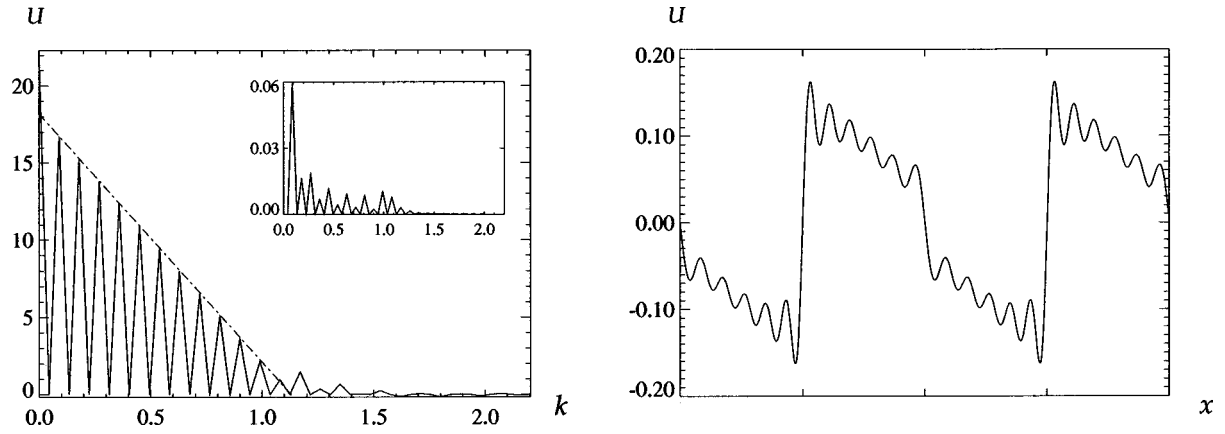

FIG. 10. Time-independent solution of the model (2.2) and (2.10). $\beta=0.005$, $\alpha=0$, and $k_1=0.09$. Left: spectrum of $z^2(k)$ ($A=2.03$, $B=18.2$, and $C=16.1$). Inset: spectrum of $|U_d(k)|$. Right: real-space numerical solution: $U_d(x)$.

$$k\left(\frac{\beta}{2k_1}\right)^2[2z^2(k)-z^2(k+k_1)-z^2(k-k_1)], \quad (4.12)$$

where $z^2(k)$ stands for the k component of z^2. We substitute an ansatz for $z^2(k)$:

$$z^2(k)=A^2+B(1-C|k|)\left(\sum_{n=-n_{\max}}^{n_{\max}}\delta(k-k_1n)\right) \quad (4.13)$$

and then Eq. (4.12) is equal to

$$k_1\left(\frac{\beta}{2k_1}\right)^2A^2\delta(|k|-k_1)+R, \quad (4.14)$$

where $R=c_1\delta(|k|-k_1n_{\max})+c_2\delta(|k|-k_1(n_{\max}+1))$. When $\alpha=0$, Eq. (4.14) is an exact solution for $k/k_1\leqslant n_{\max}=[(1+k_1)/k_1]$. We see in Fig. 10 a comparison of the ansatz (4.13) with the numerical solution [the coefficients A, B, and C were found by fitting the ansatz (4.13) to the numerical solution]. When $\alpha\neq 0$ there are deviations from Eq. (4.13): (i) There must be a discontinuity in the slope of $z^2(k)$ at $k=k_0$ so $(\mathcal{N}[U_d])(k_0)\neq 0$ and (ii) $\vartheta\neq 0$ and hence the $k\neq nk_1$ components are not zero but constant. A detailed discussion will be given elsewhere [22].

B. Stability of the stationary solution

As in the case of the solutions of the first kind, we examine now the stability of the stationary solution under small perturbations. Numerical integration of the model (2.2) and (2.10) shows that its stationary solution is stable inside the subspace of antisymmetric functions, when β is larger than a critical value β_c. Although $U_c(x)$ deviates from the exact solution of the model equation, we can expand the operator $\mathcal{L}+\mathcal{N}$ around it. This means that we may find several unstable directions towards the exact solution. Numerical computation of the stability matrix of $U_c(x)$ does show one such direction. However, this should not affect the qualitative understanding of the other eigenvalues, which lead to the stabilization mechanism.

In Appendix A we studied the stability of the short-wavelength solution $U_h(x)$. Since the amplitudes of the higher modes ($k>2$) of this solution decay exponentially with k, we were able to truncate the stability matrix after three modes and yet have a good approximation of the complete stability matrix. For two reasons this is not the case with $U_c(x)$. First, there are $\mathcal{O}(k_1^{-1})$ modes that do not decay exponentially and we want to check the stability of $U_c(x)$ in the limit $k_1\to 0$. Therefore, there is an infrared divergence in the number of relevant modes. On the other hand, we do not know *a priori* how many modes in the short-wavelength regime are needed to stabilize the solution. Therefore, we start with an infinitely large stability matrix and examine the dependence of the eigenvalues on the matrix size.

As in Sec. III A, we substitute in the model equation a solution of the form $U(x,t)=U_c(x)+e^{\lambda t}v(x)$, where $v(x)$ is a small perturbation. The linear eigenvalue equation for $v(x)$ is

$$\lambda v=\mathcal{T}[v]+\mathcal{L}^u[v]+\mathcal{L}^s[v]\equiv\mathcal{S}[v], \quad (4.15)$$

where the operator $\mathcal{T}$ is equal to

$$\mathcal{T}[v]=\partial_x[U_c(x)v(x)] \quad (4.16)$$

and the linear operator $\mathcal{L}$ has been split into two parts $\mathcal{L}=\mathcal{L}^u+\mathcal{L}^s$, where $\mathcal{L}^u$ contains only unstable modes, $L^u(k)=0$ for $|k|\geqslant 1$, and $\mathcal{L}^s$ contains only stable modes.

Since $U_c(x)$ is periodic with period k_1 [cf. Eq. (4.5)], the eigenvectors of $\mathcal{T}$ are characterized by a normalized spatial frequency $q=Q/k_1$ and they have the form

$$v(x)=\sum_{n=-\infty}^{\infty}v_ne^{i(n+q)k_1x}, \quad q\in[0,1). \quad (4.17)$$

Since $\mathcal{L}$ is diagonal, the eigenvectors of $\mathcal{S}$ will have the same form. This means that we can decompose $\sigma(\mathcal{S})$, the spectrum of $\mathcal{S}$, such that $\sigma(\mathcal{S})=\Sigma_q\sigma(\mathcal{L}(q)+\mathcal{T}(q))$, where the operators $\mathcal{L}(q)$ and $\mathcal{T}(q)$ can be represented by the infinite matrices $\boldsymbol{T}(q)$ and $\boldsymbol{L}(q)$:

$$T_{ij}(q)=\beta(i+q)u_{i-j},$$

$$L_{ij}(q)=\delta_{i,j}L((i+q)k_1), \quad (4.18)$$

where u_n is defined in Eq. (4.5b).

In [22] we show that the real part of the spectrum of $(\boldsymbol{T}^{\mathrm{N}}(q)+\boldsymbol{L}^u(q))$, where $\boldsymbol{T}^{\mathrm{N}}(q)$ is the projection of $\boldsymbol{T}(q)$ on a

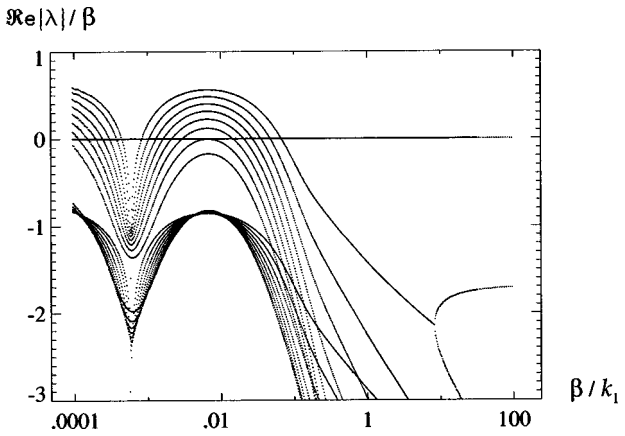

FIG. 11. Eigenvalues of the stability matrix. $k_1=1.0005/16$, $q=0$, and $\alpha=0$. Abscissa: the control parameter. Ordinate: Re$\{\lambda/\beta\}$; the real part of the largest eigenvalues of the stability matrix $\mathbf{S}(q)$ is normalized by β.

finite space of $(2N+1)$ Fourier modes $(-Nk_1,\ldots,Nk_1)$, has positive eigenvalues, but they are bounded from above by $c\ \max[\beta,\alpha(k_1/k_0)]$, where $c\sim\mathcal{O}(1)$. On the other hand, the spectrum of $\boldsymbol{L}^s(q)$ is real, negative, and unbounded from below. Then we show that for small β

$$\sigma(\boldsymbol{L}(q)+\boldsymbol{T}(q))\simeq\sigma(\boldsymbol{L}^u(q)+\boldsymbol{T}^{\mathrm{N}}(q))+\sigma(\boldsymbol{L}^s(q)), \tag{4.19}$$

where $N=\lfloor 1/k_0\rfloor$. Therefore, for small β the long-wavelength solution $U_c(x)$ is unstable. When β is increased, the coupling to the stable modes of $\boldsymbol{L}^s(q)$ stabilize the unstable modes of $(\boldsymbol{L}^u(q)+\boldsymbol{T}^{\mathrm{N}}(q))$ until $\beta=\beta_c$:

$$\frac{\beta_c}{k_1}=c\ \max\left(k_1,\frac{\alpha}{k_0}\right), \tag{4.20}$$

with $c\sim\mathcal{O}(1)$, when all the eigenvalues become negative, i.e., $U_c(x)$ becomes stable, as can be seen in the example in Fig. 11.

C. Time-periodic solution

In the preceding subsection we saw that when $\beta<\beta_c$ the stationary large-scale solution loses stability. In this subsection we describe a Hopf bifurcation of the stationary solution $U_c(x)$. We will see how the long waves and short waves interact to create a time-periodic solution. This Hopf bifurcation is the first one in a series of bifurcations that lead to a temporal chaos when β is decreased, cf. Sec. IV D.

The nonlinear model (2.2) and (2.10) conserves antisymmetry, i.e., an antisymmetric field $U(x,t_0)$ stays antisymmetric for any $t>t_0$. An antisymmetric periodic solution of frequency ω can be written in the general form

$$U_p(x,t)=m_0(x)+\sum_{n=1}^{\infty} ie^{ink_0x}[m_n(x)e^{in\omega t}+m_n^*(-x)e^{-in\omega t}] + \text{c.c.}, \tag{4.21}$$

where an asterisk denotes complex conjugation and we neglected the off-diagonal terms in (ω,k) space. We see that $m_n(x)$ are the coefficients of *left-traveling waves* and $m_n^*(-x)$ are the coefficients of *right-traveling waves*. m_0 is a stationary real function. These traveling-wave solutions break the Galilean symmetry: There is no reference system in which $U_p(x,t)$ is at rest. In order to find a periodic solution to the model equation we will have to make a few assumptions. Near the onset of a periodic solution [i.e., when $U(x)$ becomes time dependent as we decrease β] we eliminate all the $m_n(x)$ except $m_0(x)$ and $m_1(x)$. We now substitute $U_p(x,t)$ in the model equation and define

$$\mathcal{L}_{k_0}[m_1(x)]\equiv e^{-ik_0x}\mathcal{L}[m_1(x)e^{ik_0x}]. \tag{4.22}$$

The following coupled ordinary differential equations for the functions $m_0(x)$ and $m_1(x)$ are found:

$$\partial_x[\tfrac{1}{2}m_0^2(x)+|m_1(x)|^2+|m_1(-x)|^2]+\mathcal{L}[m_0(x)]=0, \tag{4.23a}$$

$$\partial_x(m_0|m_1|)+i(k_0+\partial_x\phi_1)m_0|m_1|+e^{-i\phi_1}\mathcal{L}_{k_0}[m_1]=i\omega|m_1|, \tag{4.23b}$$

where $\phi_1(x)$ is the argument of $m_1(x)$.

The exact solution for $m_1(x)$ is seen in Fig. 12. We find an approximate solution of these equations in Appendix D. We show that the onset of a periodic solution occurs at

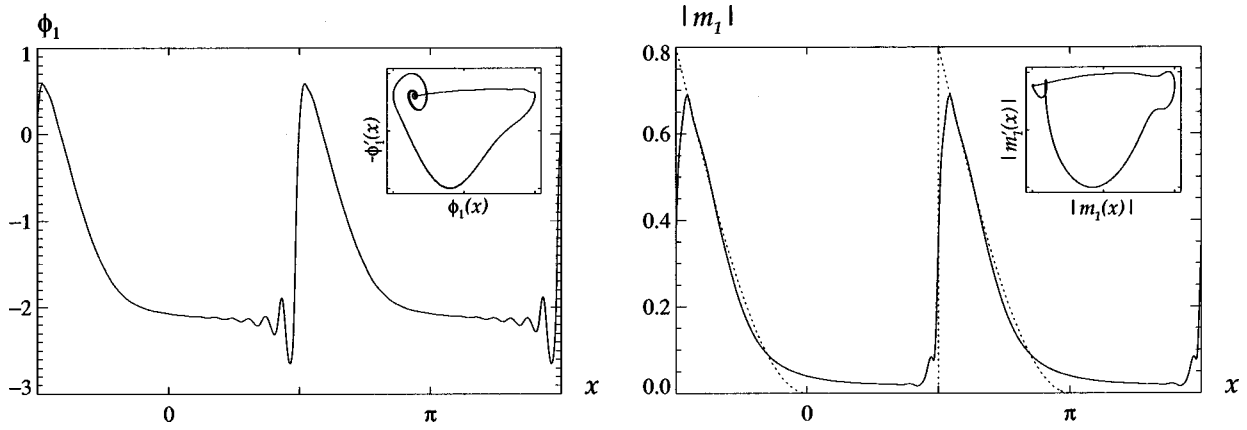

FIG. 12. Periodic solution of the model (2.2) and (2.10). $\alpha=1.2$, $\beta=0.0691$, $k_0=0.93=2\Delta k$, and $k_1=0.06$. Left: numerical solution of the phase $\phi_1(x)$. Right: numerical solution of the amplitude $|m_1(x)|$. Dotted line: analytical ansatz.

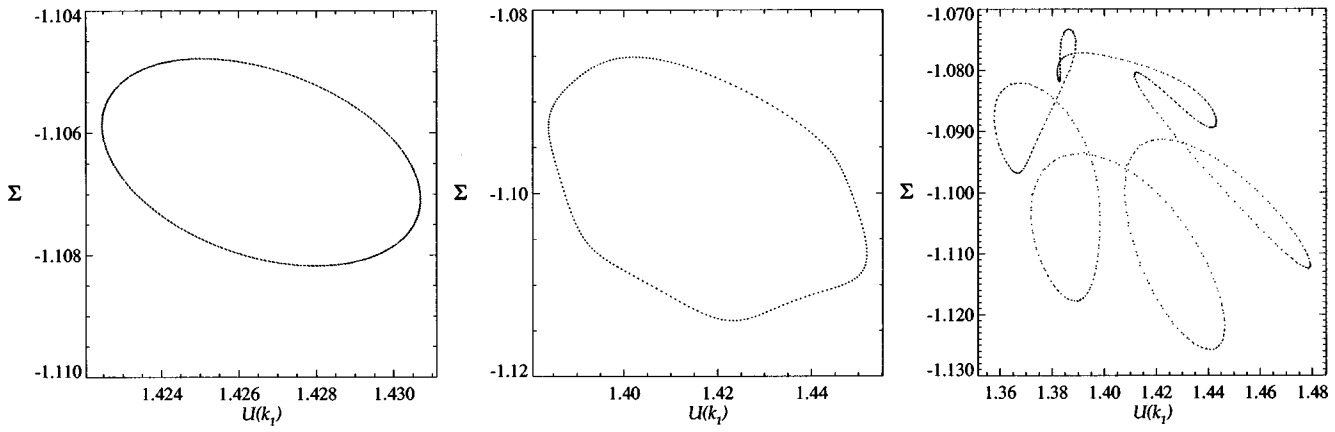

FIG. 13. Poincaré section at three values of β: 0.052 572, 0.052, and 0.0516 (left to right). $\alpha=1.2$, $k_1=0.06$, and $k_0=0.93$. The abscissa is $U(k_1)$, the amplitude of the k_1 mode. The ordinate is the square root of the total ''energy'' $\Sigma=\sqrt{\Sigma_k U(k)^2}$. The Poincaré sections were taken at $U(k_0)=0.1$.

$$\beta_c \simeq 0.0527\alpha. \tag{4.24}$$

This result is in accordance with the stability matrix estimation $\beta_c \simeq (k_1/k_0)\,\alpha$ [Eq. (4.20)]. We also find the temporal frequency of the solution

$$\omega = M_0 \frac{k_0 - k_1}{\pi - 2}. \tag{4.25}$$

In this section we analyzed the periodic solution that bifurcates from $U_c(x)$. A similar periodic solution bifurcates from $U_d(x)$, close to the bifurcation point of $U_c(x)$. So both periodic solutions coexist within the band of values of the control parameters.

D. Three modes, quasiperiodicity, and temporal chaos

The periodic solutions that we found involve left- and right-traveling waves and a stationary component. Near the onset of a periodic solution we could truncate the solution to three temporal modes: $m_1(x)e^{i(kx+\omega t)}$, $m_1^*(-x)e^{i(kx-\omega t)}$, and $m_0(x)$. As the control parameter β is decreased further, there exists a range of values for which one can still describe the temporal behavior of the model (2.2) and (2.10) by three-mode dynamics.

As an example for the β dependence consider the values $k_0=0.93$, $k_1=0.06$, and $\alpha=1.2$. Start with the stationary solution $U_d(x)$ [Eq. (4.10)]. The first Hopf bifurcation occurs at $\beta=0.0709$ and the solution becomes periodic. Starting at $\beta=0.052\,98$, we can see transient states with two frequencies ω and ω_1. The frequencies are irrational with a winding number close to 1/6. A secondary Hopf bifurcation to a quasiperiodic solution occurs at $\beta=0.052\,58$. At that point the winding number is close to 8/49 or [6,8] in continued fractions [23]. As we decrease β, harmonies of the form $m\omega+n\omega_1$, where m and n are integers, begin to appear. The phase-space ($\mathcal{U}$ space) diagram shows a T^2 torus attractor. The projection of the Poincaré section of this attractor is shown in Fig. 13. The size of the Poincaré section (Hopf radius) as a function of the distance from the bifurcation point is shown in Fig. 14.

At the bifurcation point the stationary fields $m_n(x)$ of Eq. (4.21) become time dependent:

$$m_n(x) \to m_n(x) + \eta_n(x)e^{i\Omega t} + \tilde{\eta}_n(x)e^{-i\Omega t}. \tag{4.26}$$

The linearized equation for $\eta_1(x)$ is identical to Eq. (4.23b):

$$\partial_x(m_0|\eta_1|) + i(k_0+\partial_x\phi_{\eta_1})\,\eta_0|m_1| + e^{-i\phi_{\eta_1}}\mathcal{L}_{k_0}[\eta_1] = i\omega_1|\eta_1|, \tag{4.27}$$

where $\omega_1 \equiv \omega+\Omega$ and $\phi_{\eta_1}(x)$ is the argument of $\eta_1(x)$. We write the solution in the form $m_0(x)=M_0\tilde{m}_0(x)$, $\eta_1(x)=N_1\tilde{\eta}_1(x)$ where $\tilde{m}_0(x)$ and $\tilde{\eta}_1(x)$ are some functions independent of the parameters (α,β), so when the real part of Eq. (4.27) is integrated from 0 to $\mathfrak{L}$ we get

$$N_1 + a_1 N_1 M_0 = 0. \tag{4.28}$$

The equation for $m_0(x)$ takes the form

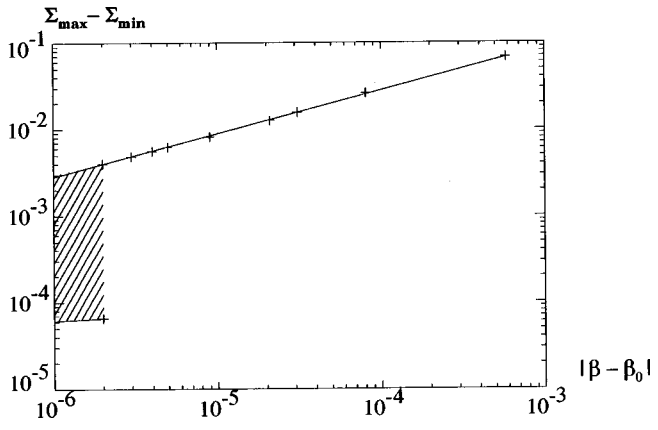

FIG. 14. Measure of the size of a Poincaré section (Hopf radius) as a function of the distance from the bifurcation point. $\alpha=1.2$, $k_1=0.06$, and $k_0=0.93$. The ordinate is the difference between the maximum and the minimum of the square root of the total energy $\Sigma=\sqrt{\Sigma_k U(k)^2}$ on the Poincaré section $U(k_0)=0.1$. In the shaded region the size of the Poincaré section depends on the initial conditions. The slope of the straight line is 0.50 and the bifurcation point is $\beta_0=0.052\,581$.

$$\partial_x\left(\frac{1}{2}m_0^2(x)+\sum_i\left[|m_i(x)|^2+|m_i(-x)|^2\right]+\left|\eta_1(x)\right|^2+\left|\eta_1(-x)\right|^2\right)+\mathcal{L}[m_0(x)]=0. \tag{4.29}$$

After projecting Eq. (4.29) on e^{ik_1x} the effective equation near the bifurcation point becomes

$$(\beta-\beta_0)M_0+b_1N_1^2=0. \tag{4.30}$$

From Eqs. (4.28) and (4.30) we find that the bifurcation of the quasiperiodic solution is supercritical:

$$N_1^2=\frac{\beta_0-\beta}{b_1a_1}, \tag{4.31}$$

as can be verified in Fig. 14.

At lower values of β a new commensurate frequency appears at $\omega_L=\omega-6\omega_1$. At $\beta=0.0519$, ω and ω_1 are exactly rational with a winding number 7/43 or [6,7]. When $\beta=0.051\,76$ the torus breaks immediately after the appearance of a new incommensurate frequency $\omega_2<\frac{1}{2}\omega_L$ and the Poincaré section becomes chaotic (temporal chaos). When we further decrease β, one eigenvalue again becomes negative and we find a new T^2 torus at $\beta=0.0516$. The system once more becomes chaotic at $\beta\leqslant 0.0515$. This behavior is in agreement with the picture found in Sec. IV B (see Fig. 11).

The bifurcations of the system were also checked at $\alpha=0.45$ and a variant of the above scenario was found. A period-2 solution appears at $\beta=0.0316$. A T^2 torus is excited at $\beta=0.0305$. The torus undergoes a period-doubling bifurcation at $\beta=0.0288$ and it becomes chaotic at $\beta=0.028\,75$. An ordered torus reappears at $\beta=0.0287$ and becomes again chaotic at $\beta=0.0286$. Notice that the stationary solution itself is stable down to $\beta=0.029$ (hysteresis). Using the two control parameters β and α, we can find a variety of winding numbers: For example, when $\beta=0.075$ and $\alpha=1.9$, we find a mode locking with a winding number of 1/5. One can study the quasiperiodic band in the (α,β) parameter space (see Fig. 15) and look for universal properties [24–26].

E. Summary

In this section the U_{II} family of large-scale solutions was introduced and discussed. We found two stationary solutions that were denoted $U_c(x)$ and $U_d(x)$. These solutions are stable when $\beta>\beta_c$. As β is decreased, the stationary solutions undergo a series of Hopf bifurcations and become periodic, quasiperiodic, and then temporally chaotic. The first Hopf bifurcation is subcritical; the stationary solution is stable for a band of parameters below the line of transition to the periodic orbit. We interpret this scenario as a *Ruelle-Takens phenomenon* [27,28]. The time-dependent solutions are composed from patches of short wavelength, left- and right-traveling waves, separated by sources and sinks, on a background of the stationary long-wavelength solution. Notice that at any given values of the control parameters there are two distinct ordered or temporally chaotic trajectories.

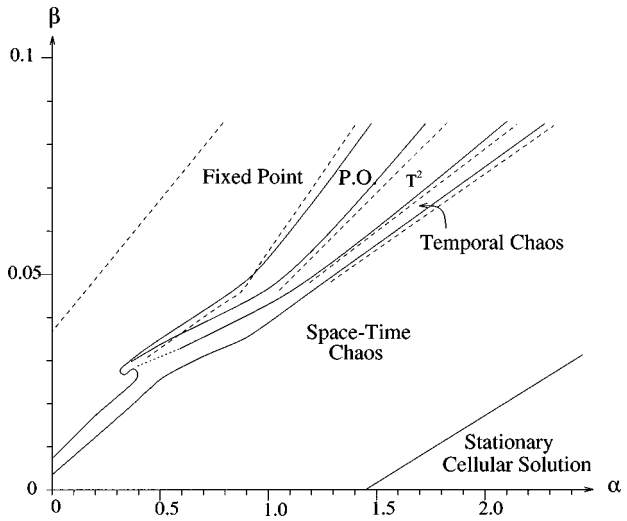

FIG. 15. Schematic phase diagram of the *two-mode model* at $k_0=0.93$ and $k_1=0.06$. The solid lines show bifurcations of $U_c(x)$ from a fixed point to a periodic orbit, T^2 torus, temporal chaos, and space-time chaos. The dashed lines refer to the same bifurcations in $U_d(x)$. Notice that $U_d(x)$ does not exist to the left of the leftmost dashed line.

When β is lowered further we expect two things to happen: (i) The number of unstable directions grows and at $\beta\gtrsim 0$ it is proportional to the effective system size k_1^{-1} and (ii) the amount of phase space that is visited by the chaotic trajectories is expected to grow as β is decreased.

V. QUALITATIVE FEATURES OF THE SPATIOTEMPORAL COMPLEX DYNAMICS

This section, which is the least rigorous in this paper, offers a qualitative description of the dynamics that leads to spatiotemporal complexity. We use here all the results found in Secs. III and IV to portray the itinerary of a typical orbit in functions space $\mathcal{U}$. In addition, we describe below additional numerical experiments to support the qualitative concepts that are offered. We begin with such a numerical description of a typical trajectory.

A. Transition to space-time chaos

To obtain a global picture of the structure of the phase space we need first to choose how to represent trajectories in our infinite-dimensional phase space. Two useful coordinates that give comprehensible projections can be constructed. The first is $U(k_0)$, the amplitude of the k_0 mode. The second is the square root of the ''energy'' of all the other modes in the unstable region

$$\Lambda=\sqrt{\sum_{0<k<1,k\neq k_0}U(k)^2}. \tag{5.1}$$

The reduction to two coordinates is done because of graphical convenience. However, the choice is also justified by the findings of the earlier sections; the U_I family emanates from the single unstable mode at k_0. The modes with $k>1$ are slaved to the modes in the sum (5.1).

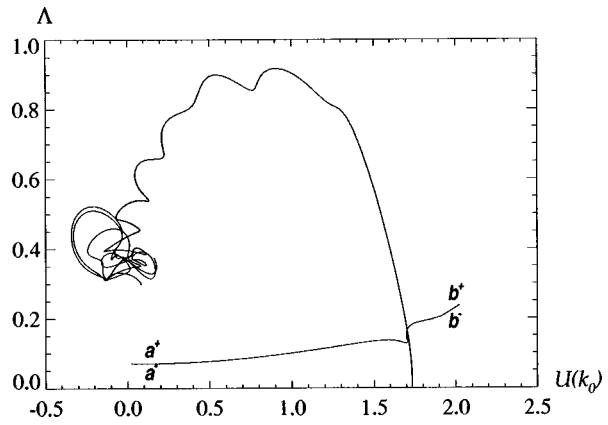

FIG. 16. Reduced representation of four trajectories in the phase space $\mathcal{U}$. The abscissa is $U(k_0)$, the amplitude of the k_0 mode. The ordinate is defined in Eq. (5.1). The initial conditions a^- and b^- flow to the fixed point $U_h(x)$ ($\Lambda=0$), while a^+ and b^+ become chaotic. $k_0=0.93$, $\alpha=0.3$, and $\beta=0$.

In this representation the stationary solution $U_h(x)$ [Eq. (3.1)] is located on the abscissa $\Lambda=0$. We saw in Sec. III A that the stationary cellular solution $U_h(x)$ is stable when $\alpha>\alpha_{\rm ext}$. Numerical experiments show that when $\beta<\beta_{\rm min}(\alpha;k_0,k_1)$, a spatiotemporal chaotic phase exists beside the ordered phase $U_h(x)$. In Fig. 16 one can see the results of four runs with different initial conditions: Two trajectories (a^- and b^-) flow to the fixed point $U_h(x)$, while the other two exhibit spatiotemporal chaotic behavior. These examples are generic. There are two gross ''basins of attraction'' here. One region flows to the fixed point $U_h(x)$ and the other region spawns chaotic orbits. Further detailed analysis of the second region reveals the existence of other small basins of attraction of additional fixed points dispersed inside it. These will be referred to below.

To establish the existence of sharp separatrix in this space we chose a random direction in phase space $\hat{R}$ and started the orbit from the ''noisy initial condition'' chosen as a linear combination of the cellular solution and the random direction

$$U(k,t=0)=A_hU_h(k)+A_r\hat{R}. \tag{5.2}$$

The model consisting of Eqs. (2.2) and (2.10) and $\beta=0$ was then integrated in time and we checked whether the chaotic or the ordered phase was obtained. We repeated the integration for a set of initial conditions, different values of A_r, fixed value of A_h, and various values of the system size $\mathfrak{L}$. Notice that the hyperplane $U(k_0)=0$ is a critical plane, i.e., when the initial conditions are $A_h>0$ [$A_h<0$], then the trajectory first grows in the $U(k_0)>0$ [$U(k_0)<0$] half plane, as can be seen in Fig. 16. The results of the numerical experiments are shown in Fig. 17. We see that there is a sharp phase transition between the ordered and chaotic phases. We also see that below $\alpha\simeq0.25$ the cellular solution is unstable. This is in agreement with the stability matrix result $\alpha_{\rm ext}=0.2475$ (at $k_0=0.93$;, see Fig. 3). Above $\alpha_{\rm ext}$ the transition line scales like

$$A_r=a(\mathfrak{L})(\alpha-\alpha_0)^\gamma. \tag{5.3}$$

The transition line and the phase-space trajectories suggest that there is an unstable fixed point in the phase space whose stable manifold separates the basin of attraction of the fixed point $U_h(x)$ and the chaotic orbit. Actually, we found in the numerical experiments a family of such fixed points. These biperiodic fixed points are characterized by two wave numbers k_0 and its subharmonic $Q=k_0/s$ ($s\in\mathbb{Z}$, $Q>1-k_0$). An example with $s=11$ is shown in Fig. 18. The exact biperiodic solutions $U_h^{(s)}(x)$ that we found in Sec. III E can be realized in a numerical experiment only if the basic spatial frequency of the solution k_0/s is a multiple of the smallest frequency $2\pi/\mathfrak{L}$. Generally this is not the case and the numerical integration shows only a close approximation to $U_h^{(s)}(x)$. An example of this finite size effect may be seen in Fig. 18. The stationary solution $U_h(x)$ has $k_0/\Delta k=31$ cells. The spectral picture shows a period-11 solution, but the lowest excited spatial mode is mode number $\lfloor 31/11\rfloor=2$. Accordingly, the real-space picture shows two basic blocks. A fixed point with a specific value of s is chosen in the numerical integration due to the existence of a Q component in the initial conditions.

The biperiodic solutions $U_h^{(s)}(x)$ have only one unstable direction. These solutions are the unstable fixed points that have been recognized in the numerical experiments. The

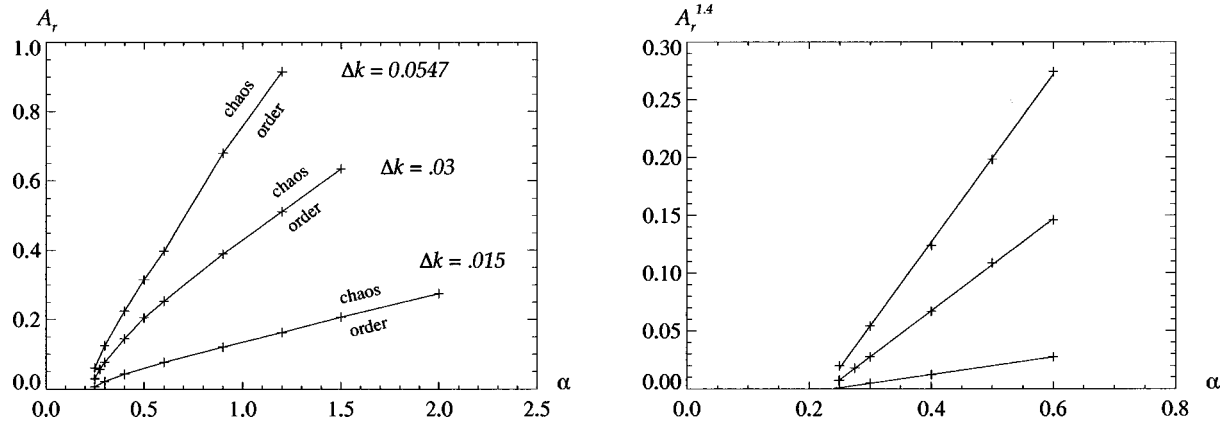

FIG. 17. Phase transition between chaotic and ordered phases as a function of the initial condition [$A_h=2$; see Eq. (5.2)] for different values of α and $\mathfrak{L}=2\pi/\Delta k$. $k_0=0.93$ and $\beta=0$. Right: fit of the points in the range $\alpha<0.6$ to the lines: $A_r^{1.4}=a(\alpha-\alpha_0)$.

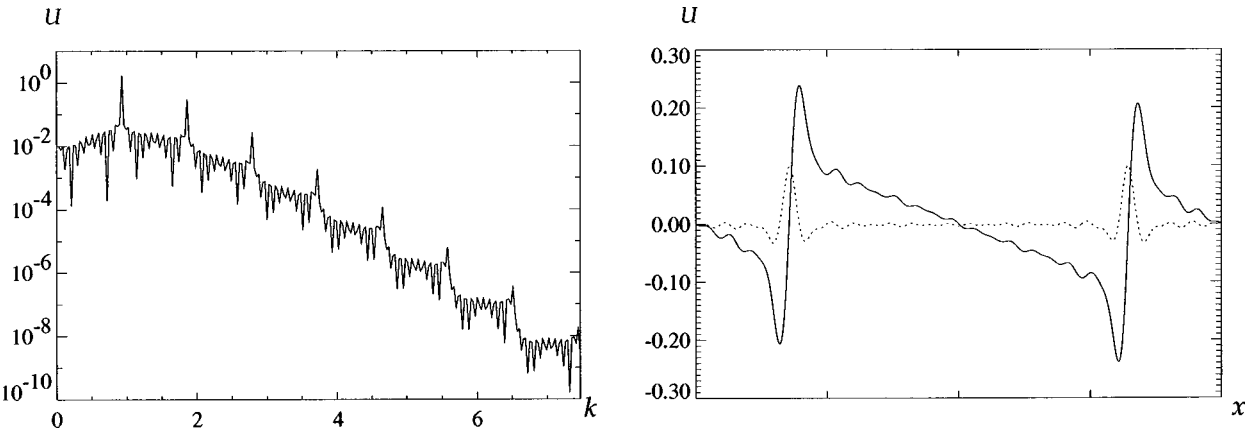

FIG. 18. Modulated cellular fixed point ($s=11$). Left: spectrum of the solution. Right: phase $\varphi(x)$ (full line) and local wave number (dotted line) (numerical experiment at $k_0=0.93$, $\alpha=0.3$, and $\Delta k=0.03$).

codimension-one stable manifold of these solutions is the separatrix between the basins of attraction of the ordered phase and the disordered phase.

The size of the basin of attraction of $U_h(x)$ is determined by the phase-space distance between $U_h(x)$ and $U_h^{(s)}(x)$. Therefore, the value of γ in Eq. (5.3) is determined by the α dependence of the largest coefficient $b_{n/s}$, where n is an integer between 1 and $s-1$. If we test this dependence in various solutions $U_h^{(s)}(x)$ we find that above the immediate vicinity of the bifurcation point, the largest coefficient scales like $(\alpha-\alpha_c)^\gamma$ where γ is in the range $0.5<\gamma<1$ and it takes different values in different biperiodic solutions.

A solution $U(x)$ in the vicinity of $U_h(x)$ can be modeled by

$$U(x)=U_h(x+\varphi(x))+W(\varphi(x)). \tag{5.4}$$

Close to $U_h(x)$, $\varphi(x)$ is small and is slowly varying in space such that $\varphi(x)=\epsilon\phi(\epsilon x)$ and $W(\varphi(x))\sim\epsilon^2$, where ϵ is a small parameter. When the amplitude of $\varphi(x)$ is small the solution relaxes towards $U_h(x)$. In Fig. 18 we see the deviation of the local wave number $d\varphi(x)/dx$ from k_0 exactly at the biperiodic fixed point. When the local wave number is too large, the solution becomes locally unstable. This long-wavelength phase instability is an Eckhaus-type instability [29] and is known in other systems [30,31] that exhibit similar phase modulation [32,16]. When the local phase deviation becomes larger, the amplitude of $U(x)$ becomes smaller and topological defects are nucleated at the points where the local wave number is too large. Immediately after the defects are created, the system leaves the vicinity of the modulated cellular fixed point and flows towards the spatiotemporal chaotic attractor, as can be seen in Fig. 16, where the behavior of the system can no longer be described by phase dynamics around the cellular solution $U_h(x)$. In other words, the spatiotemporal chaotic behavior cannot be thought of as disordered time behavior of the cellular solution.

B. Complex dynamics

In this subsection we offer an image of space-time chaos that at least for the type of models studied here can be understood as an orbit in function space that is organized by the families of stationary solutions that we identified. In doing so we do not claim that we have identified all the stationary solutions, but we believe that we have control of some pertinent families that suffice to characterize some global features of the flow. The usual signatures of space-time chaos (like topological defects) will result naturally from this dynamics. We assemble now all our findings to suggest a schematic presentation of the phase space $\mathcal{U}$; see Fig. 19. In Sec. IV D we found that the long-wavelength solutions of the U_{II} family become temporally chaotic through a series of Hopf bifurcations. The chaotic attractor stays close to a T^2 torus and it involves only few spatial components that have an erratic modulation in time. Although every component is a complicated function of space with a wide spatial spectrum, nonetheless we are still in the regime of temporal chaos. The space-time picture is one of phase turbulence around one of the long-wavelength solutions $U_c(x)$ and $U_d(x)$.

In Sec. III we studied the short-wavelength stationary solution $U_h(x)$ and a set of biperiodic solutions $U_h^{(s)}(x)$ that bifurcate from $U_h(x)$ on the neutral curve. The basin of attraction of the long-wavelength stationary solutions $U_c(x)$ and $U_d(x)$ and their time-dependent descendants is confined by the codimension-one stable manifold and the one-dimensional unstable manifold of the biperiodic fixed points $U_h^{(s)}(x)$, as can be seen schematically in Fig. 19.

The U_I family of stationary solutions has been considered in Sec. III B. Numerical examination of these fixed points shows that most of them are contained within the basin of attraction of the U_{II} family of solutions (the hatched area in

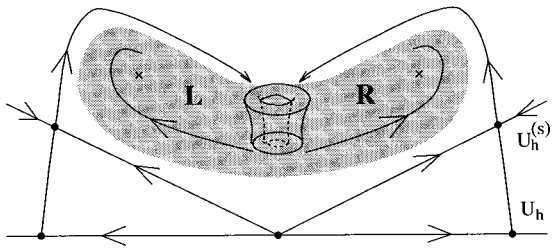

FIG. 19. Schematic presentation of the phase space $\mathcal{U}$. The torus in the center encircles a stationary fixed point (U_c or U_d). Its basin is bounded by the one-dimensional stable manifold and the unstable manifold of the biperiodic fixed points, represented here by the saddle fixed point $U_h^{(s)}$.

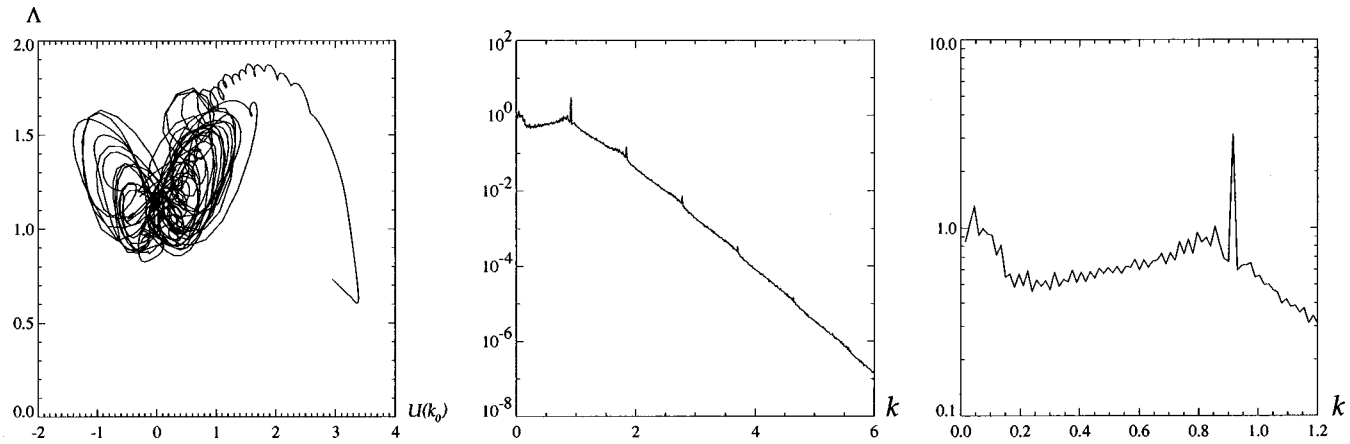

FIG. 20. Left: typical chaotic orbit at $\beta=0$. (The axes are defined in Fig. 16.) Middle: time-averaged spatial spectrum of the chaotic orbit. Right: enlargement of the long-wavelength region. $k_0=0.93$ and $\alpha=1.2$.

Fig. 19). When Δk is small enough, they are unstable (saddle fixed points). In addition to the unstable stationary solutions, there are also temporally periodic solutions inside the basin of attraction of U_{II}. For example, we found a stable periodic orbit at $\Delta k=0.037$, $k_1=2\Delta k$, $k_0=25\Delta k$, $\beta=0.03$, and α in the range 1.8–1.9. This orbit, similarly to $U_p(x,t)$ [Eq. 4.21], is composed of a stationary part and segments of left- and right-traveling waves with temporally modulated amplitude. At low values of Δk these objects lose stability.

When β is decreased below the point of transition to temporal chaos (or α is increased), the ''size'' of the chaotic attractor around the torus becomes bigger [Eq. (4.31)] until the system reaches a critical point where the chaotic attractor suddenly widens as it approaches the stable manifold of one of the saddle objects. (For $k_0=0.93$, $k_1=0.06$, and $\alpha=1.2$ it happens at $\beta\sim0.048\,55$). The trajectory spends long intervals of time in the metastable chaotic attractor near the torus, until it is attracted towards the saddle; it then bursts out and stays close to the saddle for a short period of time before returning to the former attractor, guided by the unstable manifold of $U_h^{(s)}(x)$; it remains there for a long time and then repeats the cycle.

The time interval between bursts is randomly distributed, but its average length becomes shorter as β is decreased. This phenomenon, where the chaotic attractor loses stability when it approaches an unstable (saddle) fixed point (or a periodic orbit) that is inside the attractor's basin and collides with it through a heteroclinic tangency, was called an *interior crisis* and the chaotic temporal behavior was called *crisis-induced intermittency* [33].

The space-time picture resulting from the intermittent heteroclinic connection between the temporally chaotic attractor and the saddles inside the basin is that of spatiotemporal chaos. The intermittency produces low-frequency noise in the temporal spectrum. Due to the parity symmetry, for any saddle $U_u(x,t)$ in **R** (see Fig. 19) there is a counterpart $-U_u(-x,t)$ in **L**. Accordingly, the trajectory will have the form of a doubly heteroclinic orbit as it wanders around $U_u(x,t)$, the torus, and $-U_u(-x,t)$. As β is decreased further the chaotic trajectory will discover more and more saddle objects inside its basin of attraction. A typical trajectory shape is seen in Fig. 20.

Due to the translation symmetry $U_c(x+\mathfrak{L}/4)$ is also an antisymmetric fixed-point solution of the model equation. At low values of β the chaotic tori around $U_c(x)$ and $U_c(x+\mathfrak{L}/4)$ merge. At even lower values of β, this orbit is merged with the one around $U_d(x)$ and $U_d(x+\mathfrak{L}/4)$. As the trajectory meanders between these tori, one cannot recognize the ''footprints'' of the fixed points $U_c(x)$ and $U_d(x)$ in the real-space picture, yet the averaged spectrum of the chaotic attractor retains the k^{-2} long-wavelength spectrum of the stationary solutions as can be seen in Fig. 20.

C. Explicit example

The aim of this subsection is to provide an explicit example for the picture that we offered for the nature of space-time chaos. We consider a situation that allows following the orbit as it passes close to specific stationary unstable solutions. The system undergoes bifurcations, as a function of a parameter, of the type discussed in the preceeding subsection, leading to increasing complexity in the space-time dynamics.

To allow detailed understanding of the dynamics we simplify the situation by having only few modes in the range $k\in(0,1)$. We choose arbitrarily the parameters $\Delta k=0.17$, $k_0=5\Delta k$, and $k_1=2\Delta k$. With these parameters there are precisely five unstable modes in our model. To view the trajectories we project them on the two-dimensional plane (U_1,U_5), where U_n denotes the amplitude of the mode $n\Delta k$.

At $\alpha=0$ the model equation possesses a long-wavelength solution. An approximation of this solution was calculated in Sec. IV A and denoted as $U_c(x)$. This approximation is valid as long as $\beta/k_1\geqslant1$. At lower values of β the approximation breaks down. However, in the present example, in which only a few unstable modes exist, one can calculate this solution explicitly using a truncation method of the type employed in Sec. III B. When α increases this stationary solution becomes time periodic via a Hopf bifurcation. The stationary and the periodic solutions belong to the family of solutions of the second kind that was denoted as U_{II}.

In addition, for $\beta=0$ the model equation has a short-wavelength solution denoted as $U_h(x)$ and the subharmonic solutions $U_h^{(s)}(x)$ (cf. Sec. III E and Fig. 8). For our example

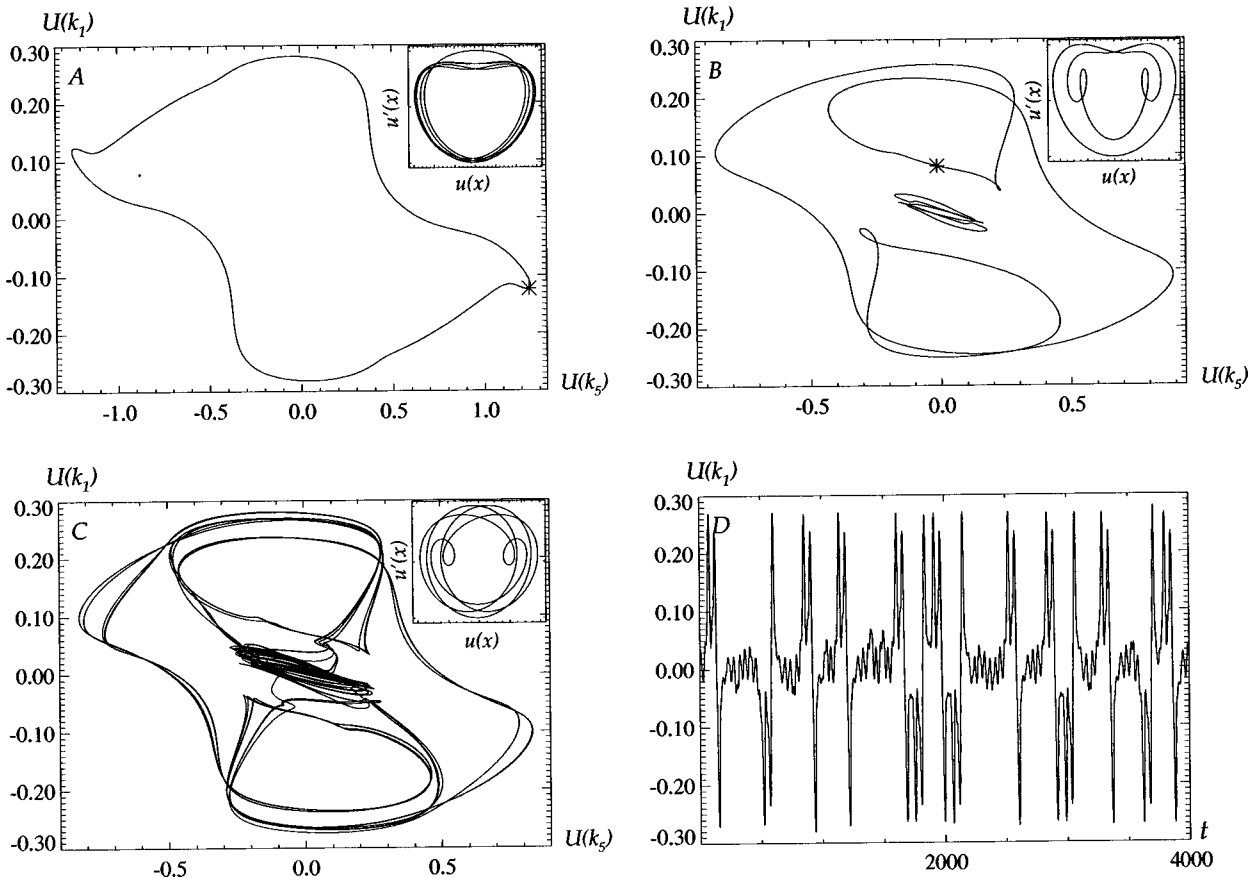

FIG. 21. (a)–(c) Reduced representation of various trajectories. Insets: spatial solutions at some emphasized points along the trajectories, shown in the (U,U') plane. (a) The periodic trajectory $U_h^{(5)}(x,t)$ ($\alpha=0.288$, $\beta=0.009\,32$). Inset: a point close to $U_h^{(5)}(x)$. (b) Two periodic trajectories that belong to the U_I family (outer, $\alpha=0.22$, and $\beta=0.0105$; inner, $\alpha=0.14$ and $\beta=0.0105$). Inset: a $p=4$ point. (c) Trajectory that connects the three solutions of the U_I family. (d) The time trace of $U(K_1)$ ($\alpha=0.22$ and $\beta=0.018$). Inset: a $p=6$ point on the inner trajectory of (b).

the only realizable solutions are $U_h^{(5)}(x)$. The pair of solutions $U_h^{(5)}(x)$ and $U_h^{(5)}(x-5\pi/k_0)$ are unstable. However, at $\alpha\approx\alpha_{\rm ext}$ (recall Sec. III A) there exists a stable periodic solution that passes near this pair of unstable stationary solutions. The projection of the trajectory of this solution is shown in Fig. 21(a). For future reference we denote this solution as $U_h^{(5)}(x,t)$. In terms of our general notation this time-dependent solution belongs to the family of solutions of the first kind U_I. The solution $U_h^{(5)}(x,t)$ remains available for a finite range of β values.

As explained in Sec. III B, the U_I family contains infinitely many solutions, all of which are unstable at $\beta=0$. For $\beta>0$ there exists a class of solutions that become stable. These are solutions whose spatial periodicity p is harmonic in k_1 (i.e., $p\Delta k/k_1$ is an integer). In the current case this condition is obtained for various values of p. For example, when $p=4$ the stationary solution $\mathbf{R}_1\mathbf{L}_0\mathbf{R}_0\mathbf{L}_1$ is stable at $\alpha=\beta\lesssim 0.001$. Note that this is one of the class of four $p=4$ solutions that appear in Eq. (3.22). At higher values of α these solutions become time periodic. At even larger values of α they become unstable.

We describe now a path in the (α,β) parameter space that begins at $\alpha=0.28$, and $\beta=0.0105$. At these values the temporal-periodic solution $U_h^{(5)}(x,t)$ is the only stable one. As α is decreased, the solution goes through dynamic bifurcations and new frequencies appear in the temporal spectrum. In addition, there exist *structural* bifurcations, where the phase-space trajectory changes its shape discontinuously. These bifurcations are understood as a consequence of the appearance of a connection between two unstable solutions: $U_h^{(5)}(x,t)$ and one of the $p=4$ class. The four members of this class interact with $U_h^{(5)}(x,t)$ at different sectors of the (α,β) plane, causing sharp changes in the character of the trajectory. At some values of α the new time-periodic orbit is stable. A typical example of such a trajectory is seen in Fig. 21(b). At other close values of α the trajectory acquires complex dynamics. Changing the parameters further one can discover orbits whose symbolic notation increases in complexity. For example, in Fig. 21(c) we see a trajectory that passes near a solution whose symbolic word is $\mathbf{R}_0\mathbf{L}_0\mathbf{R}_0\mathbf{L}_1\mathbf{R}_1\mathbf{L}_0\mathbf{R}_0\mathbf{L}_0$. It is obvious that the orbit meanders between the three solutions $U_h^{(5)}(x,t)$, $\mathbf{R}_1\mathbf{L}_0\mathbf{R}_0\mathbf{L}_1$, and the last one. The changes in the apparent spatial patterns of our time-dependent solution become more and more complex as it passes near the various unstable fixed points that are identified in this example and shown explicity as insets in Fig. 21. A time series of the total energy in this orbit is seen in Fig. 21(d). The orbit exhibits the bursts that were discussed in the previous subsections. There is no limit to how we can make the discussion more complex by choosing more modes

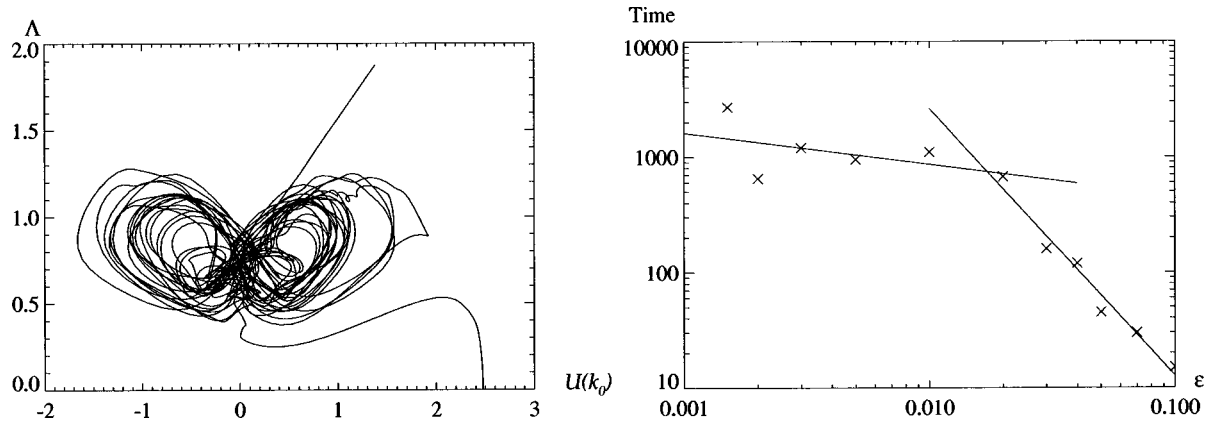

FIG. 22. Left: reduced representation of a trajectory that converges to the cellular fixed point. (The axes are defined in Fig. 16.) $\varepsilon=0.01$, $k_0=0.93$, and $\alpha=0.6$. Right: convergence time as a function of ε. We did not find convergence for $\varepsilon\leqslant 0.001$.

in the window $k\in(0,1)$. We explicitly gave the example such that the complexity can be unfolded. It is our main proposal that the space-time complexity is in principle describable in this manner.

Until now the fundamental solutions belonged to one family U_I. Continuing along our path in parameter space, we encounter new solutions that twist around members of the two different families U_I and U_{II}. These new solutions can be found by either decreasing α or increasing β.

Finally, we note that this type of solution is generic in the sense that it exists for a wide range of parameters in the (α,β) plane. It undergoes additional dynamic bifurcations as the parameters are changed further into the space-time chaotic phase. The nature of the orbit as a mediator between different types of fundamental solutions remains the same.

D. Does sustained chaos exist?

In the two-mode model the size of the attractor is a function of α and β and therefore there is a function $\alpha_c(\beta)$ such that chaos appears to exist for $\alpha<\alpha_c(\beta)$. The line representing this function is the rightmost line in the phase diagram (Fig. 15). Numerical experiments indicate that to the right of this line space-time chaos is a transient phenomenon.

Indeed, it has been suggested before [4] that all the ''chaotic'' states of the Kuramoto-Sivashinsky equation are only a long-lived transient that always relax to a stationary cellular solution. In our terminology, this means that there is no separatrix between the chaotic part of the phase space and the cellular fixed point $U_h(x)$, i.e., the chaotic part lies within the basin of attraction of the cellular fixed point.

Our models allow us to shed some light on this important issue and to show in which sense it can be assessed quantitatively. We will show that for strong linear dissipation, the chaotic state is indeed transient. To this aim consider the model

$$L(k)=\begin{cases}0, & k=0\\ -\varepsilon, & |k|<1,\ k\neq 0,\pm k_0\\ \alpha, & k=\pm k_0\\ k^2-|k|^4, & |k|\geqslant 1.\end{cases}\qquad(5.5)$$

The ε term ($\varepsilon>0$) introduces dissipation at long wavelengths ($0<k<1$) but leaves the model Galilean invariant. Starting from the initial conditions (5.2), the equation was integrated and the trajectory followed. A typical trajectory and convergence times for various values of ε are shown in Fig. 22. We found that for $\varepsilon>\varepsilon_c=0.001$ the trajectory always converged to the time-independent cellular solution $U_h(x)$. For $0\leqslant\varepsilon\leqslant\varepsilon_c$ the trajectories did not converge until at least $T=10\,000$. These results indicate that when there is enough dissipation in the long-wavelength region the chaotic state is indeed transient.

This phenomenon is common to situations where there exist simultaneously a stable fixed point $[U_h(x)]$, a chaotic attractor, and a saddle fixed point $[U_h^{(s)}(x)]$. The boundary of the basin of attraction of the attractor is the stable manifold of the saddle point (see Fig. 19). As ε is increased from zero, a critical value ε_c is reached where the chaotic attractor collides with its basin of attraction (the stable manifold of the saddle fixed point) through a heteroclinic tangency. For values of ε above the critical value the chaotic attractor disappears. This phenomenon is called *boundary crisis* [33]. We conclude that our model exhibits sustained chaos as long as the size of the chaotic attractor is not too big, i.e., the attractor does not collide with the edge of its basin of attraction.

These results indicate that even at a finite but small dissipation, the chaotic attractor may not collide with the basin of the cellular fixed point. Numerical experiments of course cannot rule out the possibility of an extremely long transient. However, all simulations done to the left of the critical line in Fig. 15 produced sustained chaos for arbitrary simulation times.

VI. SUMMARY

The main point of this paper is that spatiotemporal complexity can be discussed, at least in the class of Galilean invariant models studied above, in qualitative terms not unlike those of dynamical systems. Usually partial differential equations give rise to such complex dynamics that it is hard to disentangle the behavior into its elements. For this reason we opted in this paper to introduce a simple enough model, with only two linearly unstable modes, whose dynamics in function space could be analyzed relatively easily. One important ingredient in our analysis is the calculation of the stationary solutions. There are infinitely many such solu-

tions, but we have been able to classify many of them and show that their number grows exponentially as a function of the size of the system, at least in the scaling limit of small exiting modes.

There are regions of parameter space for which all the stationary solutions in a given portion of function space are unstable. This does not mean, however, that they are irrelevant for the dynamics. On the contrary, their neighborhood is repeatedly visited by the orbit in function space. The demonstration of spatial complexity in terms of the topological entropy translated now to a statement about spatiotemporal complexity. The orbit in time as a function of time makes nearby visits to infinitely many stationary solutions that are all unstable. When the orbit comes very close to some solution the spatial function that is seen is very close to the stationary solution, but this changes in favor of another one as the orbit nears another stationary solution, etc. Transitions between solutions of two different families that are qualitatively different, such as the families of the first and the second kind discussed above, guarantee that the observed spatial shape changes wildly while the orbit goes through its gyrations. Clearly, when the orbit changes from the vicinity of the short-wavelength solutions to the vicinity of long-wavelength solutions, the inevitable phase slips that are required form topological defects will appear. These are the consequences of the spatiotemporal complexity and not vice versa [34].

ACKNOWLEDGMENTS

This work was supported in part by the Basic Research Fund of the Israel Academy of Sciences and the German-Israeli Foundation. J.P.E. was partially supported by the Minerva Center for Nonlinear Physics and the N. Bronicky fund, as well as the Fonds National Suisse.

APPENDIX A: STABILITY OF THE CELLULAR SOLUTION AND ITS DESCENDANTS

1. Stability analysis of the cellular solution

In order to check the stability of the cellular solution $U_h(x)$ as a function of the parameters α and β [see Eq. (2.10)], we introduce a small perturbation $U(x,t)=U_h(x)+v(x,t)$. Linearizing Eq. (2.2) gives the equation for $v(x,t)$:

$$\partial_t v(x,t)=\mathcal{L}[v(x,t)]+\partial_x[v(x,t)U_h(x)]. \tag{A1}$$

Since Eq. (A1) is autonomous with respect to time, its solution is of the form $v(x,t)=e^{\lambda t}v(x)$. The general solution of $v(x)$ can be written as $v(x)=e^{iQx}\tilde{v}(x)$ where $Q\in[0,k_0)$ and $\tilde{v}(x)$ has the same periodicity as $U_h(x)$. Therefore, the perturbation $v(x,t)$ has the form

$$v(x,t)=e^{\lambda t}e^{iQx}\sum_n iv_n e^{ink_0x}. \tag{A2}$$

Inserting this into Eq. (A1), we obtain the linear equations for the coefficients v_n:

$$\lambda v_l=L(lk_0+Q)v_l-(lk_0+Q)\sum_{n=-\infty}^{\infty}a_{l-n}v_n, \tag{A3}$$

and accordingly the stability matrix reads

$$\boldsymbol{S}_{l,n}(Q)=\frac{\partial v_l}{\partial v_n}=\delta_{l,n}L(lk_0+Q)-(lk_0+Q)a_{l-n},$$

$$l,n=-k_{\max},\ldots,k_{\max}. \tag{A4}$$

The stability matrix couples $2k_{\max}/\Delta k$ modes. Using only five modes $(a_{-2},\ldots,a_2)$ to calculate the stability of the cellular solution approximately, the matrix reads

$$\begin{bmatrix} L(-2k_0+Q) & -(-2k_0+Q)a_{-1} & -(-2k_0+Q)a_{-2} & 0 & 0 \\ -(-k_0+Q)a_1 & L(-k_0+Q) & -(-k_0+Q)a_{-1} & -(-k_0+Q)a_{-2} & 0 \\ -Qa_2 & -Qa_1 & L(Q) & -Qa_{-1} & -Qa_{-2} \\ 0 & -(k_0+Q)a_2 & -(k_0+Q)a_1 & L(k_0+Q) & -(k_0+Q)a_{-1} \\ 0 & 0 & -(2k_0+Q)a_2 & -(2k_0+Q)a_1 & L(2k_0+Q) \end{bmatrix}. \tag{A5}$$

The cellular solution becomes unstable when one eigenvalue of the stability matrix crosses the imaginary axis. Two special cases are $Q=0$ and $Q=k_1$. At any other value of Q the characteristic of the stability matrix can be written as a polynomial in α:

$$\sum_{n=0}^{5} f_n(k_0,Q;\lambda)\alpha^n=0. \tag{A6}$$

On the neutral curve (critical line) Re{λ}=0, f_0 is zero and hence we can find the neutral curve $\alpha=\alpha_1(Q;k_0)$ by solving Eq. (A6) to second order in α:

$$\alpha_1(Q;k_0)\simeq -\frac{f_1}{f_2}=\frac{L(-2k_0+Q)L(k_0+Q)L(2k_0+Q)}{4[(2K_0)^2-1](k_0+Q)[(2k_0+Q)L(-2k_0+Q)-(-2k_0+Q)L(2k_0+Q)]}. \tag{A7}$$

We see that α is positive only when $(1-k_0<Q<k_0)$. We conclude that (i) the system is stable against perturbations in the range $|Q|<1-k_0$ and (ii) α_1 has an extremum value, i.e., the system is stable against any perturbation when $\alpha>\alpha_{\rm ext}(k_0)$. The solution of Eq. (A6) to third order in α has two branches where one branch behaves like the second-order solution and there is a gap between its maximum and the minimum of the second branch at

$$\alpha_2(Q=0;k_0)\simeq 2k_0^2[(2k_0)^2-1]. \tag{A8}$$

Our basic model is invariant under parity: $Q\to -Q$. Since a $-Q$ perturbation is equivalent to a k_0-Q perturbation, the neutral curve must be symmetric around $Q=k_0/2$ and therefore $\alpha_{\rm ext}=\alpha_1(k_0/2;k_0)$.

The stability matrix is singular when $Q=0$ since $L(\pm k_0+Q)=\alpha\delta(Q)$. As a result, the matrix acquires a second zero eigenvalue. This eigenvalue manifests the Galilean symmetry of the model equation.

Numerical calculation of the eigenvalues of the stability matrix for the $Q\neq k_1$ case was done using seven modes $(a_{-3},\ldots,a_3)$, as can be seen in the example in Fig. 3. Adding higher modes to the calculation does not change the neutral curve significantly.

When $Q=k_1$ one should add the contribution of $L(Q)=\beta$ to the stability matrix. Numerical calculation shows that the eigenvalues are in the negative half plane, when $\alpha>\alpha_1(k_1,k_0)$ and $\beta<\beta_0(\alpha;k_1,k_0)$. An example can be seen in Fig. 3. We conclude that the fixed point U_h is stable when $\alpha>\alpha_{\rm ext}(k_0)$ and $\beta<\beta_0(\alpha;k_1,k_0)$.

Before we continue, let us look at the behavior of the eigenvalues of the stability matrix as a function of the two parameters α and Q $(Q\neq k_1)$. On the line $Q=0$ there are two zero eigenvalues respecting the two symmetries of the model equation: translation and Galilean. Because of the translation symmetry there is a row of zeros in the stability matrix $[\boldsymbol{S}_{0,n}(0)=0]$ that contributes one zero eigenvalue λ_t. This symmetry is continuous and when Q deviates from zero, λ_t follows Q continuously; first λ_t becomes negative and then it changes sign on the neutral curve. The second symmetry is Galilean symmetry. This symmetry yields another zero eigenvalue λ_g. However, this symmetry is discrete in our model and when $|Q|\geqslant 0$, λ_g leaps to a negative value of the order of $-\alpha$ and it stays negative for any $|Q|>0$.

2. Stability of the period-2 solution

The stability of the period-2 solution $U_h^{(2)}(x)$ can be tested using the same method that has been used to calculate the stability of the solution $U_h(x)$. At the bifurcation point the stability matrix $\boldsymbol{S}^{(2)}$ can be written as a combination of two uncoupled matrices

$$\boldsymbol{S}^{(2)}_{m/2,n/2}(Q)=\begin{cases}\boldsymbol{S}_{m/2,n/2}(Q) & \text{for } m,n \text{ even}\\ \boldsymbol{S}_{(m-1)/2,(n-1)/2}\left(Q+\dfrac{k_0}{2}\right) & \text{for } m,n \text{ odd}\\ 0 & \text{for otherwise,}\end{cases} \tag{A9}$$

where $\boldsymbol{S}(Q)$ is the stability matrix (A4). Accordingly, the eigenvalues of the matrix $\boldsymbol{S}^{(2)}(0)$ are the union of the set of eigenvalues of the matrices $\boldsymbol{S}(0)$ and $\boldsymbol{S}(k_0/2)$. $\boldsymbol{S}(0)$ has a translation zero eigenvalue λ_t and a Galilean zero eigenvalue λ_g (see the preceding section). At the same point $\boldsymbol{S}(k_0/2)$ has only one zero eigenvalue λ_t. When α is increased above the bifurcation point (and $Q=0$), the degeneracy of the two zero eigenvalues is removed and one of them becomes positive. When $|Q|$ is increased, the values of the λ_g change discontinuously to a negative value while λ_t changes its value in a continuous way. The global stability picture of $U_h^{(2)}$ is similar to that of U_h. In the (α,Q) parameter space there is a neutral curve $\alpha_1^{(2)}(Q;k_0)$, where the upper eigenvalue λ_t crosses the imaginary axis. However, in contrast to U_h (Fig. 3), the unstable region is *above* the neutral curve and therefore $U_h^{(2)}$ is unstable at any value of α.

$\alpha_1^{(2)}(Q;k_0)$, like $\alpha_1(Q;k_0)$, has an extremum at $\alpha_{ext}^{(2)}=\alpha_1^{(2)}(k_0/4;k_0)$. At that point, a secondary period-doubling bifurcation to a new solution $U_h^{(2^2)}(x)=\Sigma_n ib_{n/4}e^{i(n/4)k_0x}$ takes place. As with $\boldsymbol{S}^{(2)}$ [Eq. (A9)], at the bifurcation point the stability matrix of the new solution $\boldsymbol{S}^{(2^2)}$ can be decomposed into four matrices: $\{\boldsymbol{S}^{(2)}[Q+n(k_0/4)],n=0,1,2,3\}$. $\boldsymbol{S}^{(2)}(Q)$ contributes one zero eigenvalue λ_t, but it also contributes a positive eigenvalue λ_g. Accordingly, beyond the bifurcation point there will be one positive eigenvalue and the *second* eigenvalue will cross the imaginary axis on the neutral curve $\alpha_1^{(2^2)}(Q;k_0)$.

3. Stability analysis of the period-three solution

We will show here that the solution $U_h^{(3)}(x)$ has zero eigenvalues at α_c and α_0 [see Eq. (3.43)], as in transcritical bifurcations of low-dimensional dynamical systems (ordinary differential equations). However, in contrast to low-dimensional dynamical systems, $U_h^{(3)}(x)$ is unstable at all values of the control parameter α. Like the stability matrix of $U_h(x)$ [Eq. (A4)], the stability matrix $\boldsymbol{S}(Q)$ at a point $\alpha=\hat{\alpha}$ is defined by

$$\boldsymbol{S}_{l,n}(Q)=\delta_{l,n}L(lk_0/3+Q)-(lk_0/3+Q)b_{l-n}(\hat{\alpha}). \tag{A10}$$

We also define $\boldsymbol{B}=\boldsymbol{S}(0)$. When $\hat{\alpha}>\alpha_0$, $U_h^{(3)}$ can be expanded near $\hat{\alpha}$: $U_h^{(3)}(\alpha)=U_h^{(3)}(\hat{\alpha})+(\alpha-\hat{\alpha})\boldsymbol{v}$. $\boldsymbol{v}$ is the solu-

tion of the equation $\boldsymbol{B}\boldsymbol{\nu}=\boldsymbol{b}_1$, where $\boldsymbol{b}_1=(0,0,b_1(\hat{\alpha}),0,0,\ldots)$. That equation has a solution only if the solvability condition $\boldsymbol{b}^{\dagger}\boldsymbol{b}_1=0$ holds, where $\boldsymbol{b}^{\dagger}$ is the zero left eigenvector of $\boldsymbol{B}$. If $\boldsymbol{B}$ has a nontrivial zero eigenvector, then generically $(\boldsymbol{b}^{\dagger})_1 \neq 0$ and therefore $\boldsymbol{b}^{\dagger}\boldsymbol{b}_1=(\boldsymbol{b}^{\dagger})_1 b_1(\hat{\alpha})\neq 0$. Therefore, when $\hat{\alpha}>\alpha_0$, $\boldsymbol{B}(\hat{\alpha})$ has a zero eigenvalue only at the bifurcation point $\hat{\alpha}=\alpha_c$ where $(\boldsymbol{b}^{\dagger})_1=0$. Due to the parity symmetry $\boldsymbol{B}(\alpha_c)$ has two zero eigenvectors [equivalently, at α_c, $U_h(x)$ is unstable to two perturbations $Q=k_0/3$ and $Q=\frac{2}{3}k_0$]. The two zero eigenvalues cross the imaginary axis in opposite directions, as a function of $\alpha-\alpha_c$:

$$\left.\frac{\partial\ \mathrm{Re}\{\lambda^{+}\}}{\partial(\alpha-\alpha_c)}\right|_{\alpha_c}>0, \quad \left.\frac{\partial\ \mathrm{Re}\{\lambda^{-}\}}{\partial(\alpha-\alpha_c)}\right|_{\alpha_c}<0. \tag{A11}$$

Therefore, $U_h^{(3)}(x)$ is unstable on both sides of α_c.

When $\hat{\alpha}=\alpha_0$ the expansion of $U_h^{(3)}$ is $U_h^{(3)}(\alpha)=U_h^{(3)}(\hat{\alpha})+(\alpha-\hat{\alpha})^{0.5}\boldsymbol{v}$. Then $\boldsymbol{v}$ is the solution of the eigenvalue equation $\boldsymbol{B}\boldsymbol{\nu}=0$ with the normalization condition $\Sigma_l v_{1+l/3}v_{-l/3}=b_1(\hat{\alpha})$. Therefore, one eigenvalue of $\boldsymbol{B}(\hat{\alpha})$ changes sign at α_0. Yet λ^{-} is still positive at α_0 and therefore $U_h^{(3)}(x)$ is unstable. In addition to these two isolated zero eigenvalues, $\boldsymbol{S}(0)$ has two zero eigenvalues at any α due to the translation symmetry. One of the zero eigenvalues stays away from zero when $Q\neq 0$. We conclude that the period-3 solution $U_h^{(3)}(x)$, similarly to the period-2 solution, is unstable at any value of α.

APPENDIX B: AN $S=M=5$ SOLUTION OF THE U_{II} FAMILY

We start by looking for $m=5$ solutions with the same symmetry. We truncate the set of equations after $2(m-1)$ modes, assuming that the higher modes are much smaller than the first eight modes. To lowest order in α we assume for these modes

$$b_{n/5}=\begin{cases}\sqrt{\dfrac{\alpha}{k_0}}\,c_n & \text{for } n \text{ odd}\\ \dfrac{\alpha}{k_0}d_n & \text{for } n \text{ even,}\end{cases} \tag{B1}$$

where the c_n and d_n are functions of k_0 only. The equations for the $\frac{2}{5}$th and $\frac{4}{5}$th modes have three solutions:

$$c_1=(1\pm\sqrt{3})c_3, \quad c_5=c_3, \tag{B2a}$$

$$c_3\neq 0, \quad c_1=c_5=0. \tag{B2b}$$

Solution (B2b) is similar to solution (3.7) in the sense that its principal spatial frequency is not k_0 but $\frac{3}{5}k_0$. We will ignore that solution for the time being. If we assume $c_7 \ll c_n (n=1,\ldots,5)$, then the equations for the $\frac{6}{5}$th and $\frac{8}{5}$th modes give

$$d_8 L_8=\frac{d_6 L_6}{\frac{3}{2}\pm\sqrt{3}}=(c_3)^2, \tag{B3}$$

where

$$L_n\equiv L\left(\frac{n}{5}k_0\right)\Big/\frac{n}{5}k_0=\left(\frac{n}{5}k_0\right)-\left(\frac{n}{5}k_0\right)^3. \tag{B4}$$

Now we substitute Eq. (B3) into the equations for the $\frac{1}{5}$th, $\frac{3}{5}$ th, and $\frac{5}{5}$th modes and we get a system of three equations to solve:

$$\begin{pmatrix} 2\pm\sqrt{3} & 2 & 1\\ \pm\sqrt{3} & -(1\pm\sqrt{3}) & -(1+H)\\ 1 & 1\pm\sqrt{3} & -(1\pm\sqrt{3}+H)\end{pmatrix}\begin{pmatrix} d_2\\ d_4\\ d_6\end{pmatrix}=\begin{pmatrix} 0\\ 0\\ 1\end{pmatrix}, \tag{B5}$$

where the value of H is equal to

$$H=\frac{1}{\frac{3}{2}\pm\sqrt{3}}\frac{L_6}{L_8}. \tag{B6}$$

Substituting the solution of Eq. (B5) into Eq. (B3) determines the numerical values of the c_n. Now we can calculate d_7 from the equation for the $\frac{7}{5}$th mode and check that it is indeed negligible. Like the $m=3$ example, which has a solution only for $k_0>3/4$, Eq. (B5) has a solution only when L_6 is positive, i.e., $k_0>5/6$.

The two solutions found are shown in Fig. 5. Similar $m=5$ solutions exist for $s=3$ and $s=1$. The only difference is on the right-hand side of Eq. (B5), which is (0,1,0) for $s=3$ and (1,0,0) for $s=1$. No solutions of that type exist for $s=4$ and $s=2$.

In addition to the two period-5 solutions that were found, there are two additional solutions $U(x)$ and $\bar{U}(x)$ that can be paired such that $\mathcal{R}_2[U(x)]=\bar{U}(x)$. We will assume now that their scaling is

$$b_{n/m}=\alpha^{1/2+(1/2)\lfloor(|n|-1)/m\rfloor}c_n. \tag{B7}$$

The lowest-order equations for the $b_{1/5},\ldots,b_{4/5}$ modes have a solution

$$b_{2/5}=\sqrt{2}b_{1/5}, \quad b_{3/5}=\frac{1}{\sqrt{2}}b_{1/5},$$

$$b_{4/5}=-b_{1/5}, \quad b_{5/5}=\left(1+\frac{1}{\sqrt{2}}\right)b_{1/5}. \tag{B8}$$

The lowest-order terms in the nonlinear part of the equation for the $b_{5/5}$ mode are

$$b_{1/5}b_{4/5}+b_{2/5}b_{3/5}. \tag{B9}$$

According to the scaling *Ansatz* (B7), these terms are of order α, while the linear part is of order $\alpha^{3/2}$. However, by virtue of the relations (B8) the expression (B9) is exactly zero. Hence the amplitude of the solution is determined by the next-order terms in the equation for the $b_{5/5}$ mode:

$$b_{6/5}+\sqrt{2}b_{7/5}+\frac{1}{\sqrt{2}}b_{8/5}-b_{9/5}+\left(1+\frac{1}{\sqrt{2}}\right)b_{10/5}$$
$$=-\left(1+\frac{1}{\sqrt{2}}\right)\frac{\alpha}{k_0}. \tag{B10}$$

The equations of the $b_{6/5},\ldots,b_{10/5}$ modes, to first order in α, give

$$b_{6/5}=-\left(\frac{5-2\sqrt{2}}{4}\right)\frac{1}{L_6}b_{1/5}^2, \quad b_{7/5}=-\left(1+\frac{1}{\sqrt{2}}\right)\frac{1}{L_7}b_{1/5}^2,$$
$$b_{8/5}=-\left(1+\frac{1}{\sqrt{2}}\right)\frac{1}{L_8}b_{1/5}^2, \quad b_{9/5}=\left(1+\frac{1}{\sqrt{2}}\right)\frac{1}{L_9}b_{1/5}^2,$$
$$b_{10/5}=-\left(\frac{3+2\sqrt{2}}{4}\right)\frac{1}{L_{10}}b_{1/5}^2, \tag{B11}$$

where L_n is defined in Eq. (B4). Now we substitute Eq. (B11) into Eq. (B10) and we find two solutions for $b_{1/5}$:

$$b_{1/5}=\pm\sqrt{\frac{C}{k_0^2}\alpha}, \tag{B12}$$

where the constant C is a linear function of $1/L(\frac{6}{5}k_0),\ldots,1/L(\frac{10}{5}k_0)$. This confirms the *Ansatz* (B7).

In this section we found two solutions for $s=m=5$. For any s smaller than m, Eqs. (B8) and (B11) still hold because they solve the five first-order equations for the modes $b_{1/5},\ldots,b_{5/5}$. The only difference is in the $\mathcal{O}(\alpha^{3/2})$ equation for the $b_{5/5}$ mode [Eq. (B10)], which should be replaced by an equivalent equation for the $b_{s/5}$ mode. Accordingly, the solution (B12) holds for any $s\leqslant 5$, while the value of the constant C depends on s.

APPENDIX C: EXISTENCE OF SOLUTIONS

The vector $\boldsymbol{c}$ [see Eq. (3.13)] defines an m-dimensional Euclidean subspace of the function space $\mathcal{U}$. We denote by $\mathcal{C}$ the $(m-1)$-dimensional unit sphere in $\mathbb{R}^m$. The bilinear equation

$$\phi_l(\boldsymbol{c};\mu)=0 \tag{C1}$$

does not depend on the magnitude $|\boldsymbol{c}|$. Therefore, its solution is a point on the sphere $\mathcal{C}$. This means that apparently Eq. (C1) has m conditions but only $m-1$ degrees of freedom. However, as we will see momentarily, the m equations $\phi_l(\boldsymbol{c};1)=0$ are not independent. Let us examine the scalar product

$$(\partial_x U)\boldsymbol{\phi}(\boldsymbol{c})=\sum_l lc_l\sum_{i,j}c_iM_{ij}^l c_j. \tag{C2}$$

By renaming the indices, this quantity is equal to

$$\frac{1}{3}\sum_{i,j,l}c_ic_jc_l(lM_{ij}^l+iM_{lj}^i+jM_{il}^j)$$
$$=\sum_{i,j,l}c_ic_jc_l[(l-i-j)\delta_{i+j,l}-(l-i+j)\delta_{i-j,l}$$
$$-(l+i-j)\delta_{-i+j,l}]=0.$$

Therefore, the m components of $\boldsymbol{\phi}(\boldsymbol{c};1)$ are not independent. So at $\mu=1$ Eq. (C1) has $m-1$ degrees of freedom and $m-1$ conditions to satisfy.

The quadratic form $\phi_m(\boldsymbol{c};0)$ is identically zero. It is easy to see that the $m-1$ quadratic forms $\phi_l(\boldsymbol{c};0)$, $l<m$, are *indefinite* and therefore every equation $\phi_l(\boldsymbol{c};0)=0$ has a non-trivial solution. Every quadratic equation $\phi_l(\boldsymbol{c};\mu)=0$ can be reduced by an orthogonal matrix $\boldsymbol{P}$ to the form

$$\sum_{i=1}^{h}\lambda_i\tilde{c}_i^2-\sum_{i=h+1}^{r}\lambda_i\tilde{c}_i^2=0, \tag{C3}$$

where all the λ_i are positive, $\tilde{\boldsymbol{c}}=\boldsymbol{P}\boldsymbol{c}$, r is the rank of the matrix $\boldsymbol{M}^l(\mu)$, and $1<h<r$. One can see that the solution of Eq. (C3) is an unbounded $(m-1)$-dimensional object in the Euclidean subspace $\mathbb{R}^m$ composed of one or more sheets, which passes through the origin, and therefore must intersect $\mathcal{C}$ along $(m-2)$-dimensional closed hyperlines $\mathcal{H}^l$. The solutions of $\boldsymbol{\phi}(\boldsymbol{c};0)=\boldsymbol{0}$ are the intersections of the $m-1$ hyperlines $\mathcal{H}^l$, $l<m$, which define a set $\mathcal{P}(0)$ of (zero-dimensional) points in $\mathcal{C}$. Since we already discovered that Eq. (3.18) has 2^m solutions, we conclude that the set $\mathcal{P}(0)$ contains 2^m points.

We want to check what happens to the solutions of $\boldsymbol{\phi}(\boldsymbol{c};\mu)=\boldsymbol{0}$ as μ deviates from zero. The quadratic form $\phi_m(\boldsymbol{c};\mu)$ is equal to $\mu\phi_m(\boldsymbol{c};1)$ and therefore $\phi_m(\boldsymbol{c};\mu)$ is not identically zero when $\mu>0$. However, we know that at $\mu=1$ the set of equations $\boldsymbol{\phi}(\boldsymbol{c};1)=\boldsymbol{0}$ are not independent. Therefore, if there is a solution to the $m-1$ equations $\phi_l(\boldsymbol{c};1)=0$, $l<m$, and $c_m\neq 0$ then it must also solve the mth equation $\phi_m(\boldsymbol{c};1)=0$. So if we have a solution to the $m-1$ equations $\phi_l(\boldsymbol{c};\mu)=0$, $l<m$, at any μ, and $c_m\neq 0$, then we are guaranteed that it solves $\boldsymbol{\phi}(\boldsymbol{c};\mu)=\boldsymbol{0}$ at $\mu=0$ and 1. Accordingly, we define the set $\mathcal{P}(\mu)$ as the set of solutions of the $m-1$ equations $\phi_l(\boldsymbol{c};\mu)=0$, $l<m$. (Notice that $c_m=0$ means that the periodicity p is smaller than m.) As μ is changed, the points of the set $\mathcal{P}(\mu)$ move on the sphere $\mathcal{C}$ and they can be annihilated in pairs, as can be seen in Fig. 7.

APPENDIX D: PERIODIC SOLUTIONS

In Sec. IV C we found the following coupled ordinary differential equations for the functions $m_0(x)$ and $m_1(x)$:

$$\partial_x[\tfrac{1}{2}m_0^2(x)+|m_1(x)|^2+|m_1(-x)|^2]+\mathcal{L}[m_0(x)]=0, \tag{D1a}$$

$$\partial_x(m_0|m_1|)+i(k_0+\partial_x\phi_1)m_0|m_1|+e^{-i\phi_1}\mathcal{L}_{k_0}[m_1]=i\omega|m_1|, \tag{D1b}$$

where $\phi_1(x)$ is the argument of $m_1(x)$. The complex equation (D1b) can be written as two real equations

$$\partial_x[m_0(x)|m_1(x)|]+\mathrm{Re}\{\Psi(x)e^{-i\phi_1(x)}\}=0, \quad \text{(D1c)}$$

$$[k_0+\partial_x\phi_1(x)]m_0(x)|m_1(x)|+\mathrm{Im}\{\Psi(x)e^{-i\phi_1(x)}\} = \omega|m_1(x)|. \quad \text{(D1d)}$$

The next step is to look for a solution that, similarly to the fixed point solution, has the energies of $m_0(x)$ and $m_1(x)$ concentrated at low spatial frequencies. The *Ansatz* for $m_0(x)$ is

$$m_0(x)=M_0\tilde{m}_0(x)+R_0(x),$$

$$\tilde{m}_0(x)=\sin\left(\frac{k_1}{2}x\right)w\left(\frac{k_1}{2}x\right), \quad \text{(D2)}$$

where $w(\theta)$ is defined in Eq. (4.3) and $R_0(x)$ is a small deviation. Equation (D1b) becomes an eigenvalue equation for $m_1(x)$:

$$\tilde{\mathcal{L}}(M_0)[m_1(x)]=i\omega m_1(x), \quad \text{(D3)}$$

where

$$\tilde{\mathcal{L}}(M_0)\equiv\mathcal{L}_{k_0}+M_0(\partial_x+ik_0)\tilde{m}_0(x). \quad \text{(D4)}$$

Due to the Galilean symmetry, we expect to find left-traveling waves where $m_0(x)>0$ and right-traveling waves where $m_0(x)<0$. Hence we look for $m_1(x)$ such that $|m_1(x)|\gg|m_1^*(-x)|$, where $m_0(x)>0$ and vice versa. So the ansatz for $m_1(x)$ is

$$m_1(x)=M_1\tilde{m}_1(x)+R_1(x), \quad \text{(D5a)}$$

$$\tilde{m}_1(x)=a_1(x)e^{i\phi_1(x)}d\left(\frac{k_1}{2}x\right), \quad \text{(D5b)}$$

where $R_1(x)$ is a small deviation and $d(\theta)$ is the double periodic asymmetric rectangular wave

$$d(\theta)=\begin{cases}1 & \text{if } \dfrac{\pi}{2}\leqslant\theta\leqslant\pi\\ 1 & \text{if } \dfrac{3\pi}{2}\leqslant\theta\leqslant 2\pi\\ 0 & \text{otherwise.}\end{cases} \quad \text{(D6)}$$

We see that the points $(k_1/2)x=\{0,\pi/2,\pi,3\pi/2\}$, where $|m_1(x)|=|m_1(-x)|$, are sinks and sources of traveling waves. In Fig. 12 we see the field $m_1(x)$ as it was measured from the numerical integration [35]. In order to gain an analytical understanding of the equations we must take a simple *Ansatz* for $m_1(x)$. We will use the simple analytical form

$$a_1(x)=1+\cos\left(\frac{k_1}{2}x\right)w\left(\frac{k_1}{2}x\right), \quad \text{(D7a)}$$

$$\phi_1(x)=\Phi_1 a_1(x). \quad \text{(D7b)}$$

Now we will solve Eqs. (D1) in Fourier space by substituting the *Ansätze* (D2), (D5), and (D7), calculating the Fourier transform (see Appendix E), and comparing terms of the same spatial frequency. We will start with Eq. (D1c). The $k=0$ mode of the derivative term is equal to zero and hence that mode must be zero in the $\mathrm{Re}\{\Psi(x)e^{-i\phi_1(x)}\}$ term. The antisymmetric part of this term fulfills that condition trivially. The symmetric part accomplishes the zero condition by convolving all the Fourier modes in the interval $k=[0,3]$. Consequently, it is harder to analyze the symmetric part than the antisymmetric one. Hence we will only examine the antisymmetric piece.

Near $k=0$ we can use the facts that $L_{k_0}(k)\ll L_{k_0}(0)=\alpha$ [see Eq. (D4)] and that $e^{-i\phi_1(x)}$ has only a few modes in Fourier space to estimate the antisymmetric piece by

$$\mathrm{asym}[\mathrm{Re}\{\Psi(x)e^{-i\phi_1(x)}\}]\simeq\mathrm{asym}(\mathrm{Re}\{\Psi_{k=0}e^{-i\phi_1(x)}\}) = \alpha M_1\mathrm{asym}(\mathrm{Re}\{\tilde{m}_{1,k=0}e^{-i\phi_1(x)}\}). \quad \text{(D8)}$$

The Fourier transform of an antisymmetric function is purely imaginary. Using the notation $k=n(k_1/2)$ we can rewrite the antisymmetric piece of Eq. (D1c) in Fourier space

$$M_0 n\frac{k_1}{2}\mathrm{Re}\{(\tilde{m}_0|\tilde{m}_1|)_n\}\simeq\frac{1}{2}\alpha\mathrm{Im}\{\tilde{m}_{1,k=0}(e^{-i\phi_1})_n + [\tilde{m}_{1,k=0}(e^{-i\phi_1})_{-n}]^*\}. \quad \text{(D9)}$$

Defining C_n and $D_n(\Phi_1)$ by

$$C_n\equiv n(\tilde{m}_0|\tilde{m}_1|)_n, \quad \text{(D10a)}$$

$$D_n(\Phi_1)\equiv\tilde{m}_{1,k=0}(e^{-i\phi_1})_n+[\tilde{m}_{1,k=0}(e^{-i\phi_1})_{-n}]^*, \quad \text{(D10b)}$$

we can rewrite Eq. (D9) for any mode n as

$$M_0\frac{k_1}{\alpha}\simeq\frac{\mathrm{Im}\{D_n(\Phi_1)\}}{\mathrm{Re}\{C_n\}}. \quad \text{(D11)}$$

In particular,

$$\frac{\mathrm{Im}\{D_2(\Phi_1)\}}{\mathrm{Re}\{C_2\}}=\frac{\mathrm{Im}\{D_4(\Phi_1)\}}{\mathrm{Re}\{C_4\}}. \quad \text{(D12)}$$

Now we can solve Eq. (D12) numerically [36], using the *Ansätze* (D2) and (D7) to find Φ_1. A solution is

$$\Phi_1=2.77. \quad \text{(D13)}$$

Substitution of this result back into Eq. (D11) gives

$$M_0=\frac{\alpha}{k_1}\frac{\mathrm{Im}\{D_2(\Phi_1)\}}{1/3\pi}=\frac{\alpha}{k_1}(3\pi)(0.019). \quad \text{(D14)}$$

We turn now to Eq. (D1a). We can rewrite it as

$$\frac{1}{2}M_0^2\partial_x[\tilde{m}_0^2(x)]+M_0\mathcal{L}[\tilde{m}_0(x)]=-\partial_x\left(\frac{1}{2}R_0^2(x)+M_0\tilde{m}_0R_0 + \left|m_1(x)\right|^2+\left|m_1(-x)\right|^2\right). \quad \text{(D15)}$$

At the onset of a periodic solution the right-hand side is zero. Using Eq. (E4),

$$-i\frac{k_1}{8}M_0^2+i\frac{4\beta_c M_0}{3\pi}=0. \tag{D16}$$

So the onset of a periodic solution occurs at

$$\beta_c=\frac{3\pi}{32}k_1M_0\simeq 0.0527\alpha. \tag{D17}$$

This result is in accordance with the stability matrix estimation $\beta_c=(k_1/k_0)\alpha$. The last step is to calculate ω from Eq. (D1d). For small n we can approximate it by

$$(k_0-k_1)(m_0|m_1|)_n=\omega|m_1|_n. \tag{D18}$$

Equations (E6) and (E7) for the $n=1$ mode give

$$\omega=M_0\frac{k_0-k_1}{\pi-2}. \tag{D19}$$

We can compare now the analytic results to a numerical simulation. With simulation parameters ($k_0=0.93$, $k_1=0.06$, $\alpha=1.2$) we obtained

	M_0	ω	β_c
analytic	3.6	2.74	0.064
numerical	3.8	2.87	0.0691

We see that although the estimate (D7) for $m_1(x)$ is crude, the analytical results are close to the values from the numerical integration.

APPENDIX E: FOURIER TRANSFORM OF SOME RELEVANT FUNCTIONS

In the periodic solution the smallest spatial frequency is $k_1/2$. Hence the only relevant spatial frequencies are $k=n(k_1/2)$.

$w[(k_1/2)x;\vartheta]$:

$$A_n(\vartheta)=\begin{cases}-\dfrac{2}{\pi}\vartheta, & n=0\\ -\dfrac{2}{n\pi}\sin\left[n\left(\dfrac{\pi}{2}-\vartheta\right)\right], & n\neq 0.\end{cases} \tag{E1}$$

$d[(k_1/2)x;\vartheta]$:

$$A_n(\vartheta)=\begin{cases}\dfrac{1}{2}, & n=0\\ -\dfrac{i}{n\pi}\cos\left[n\left(\dfrac{\pi}{2}-\vartheta\right)\right], & n \text{ odd}\\ -\dfrac{i}{n\pi}\left\{\cos\left[n\left(\dfrac{\pi}{2}-\vartheta\right)\right]-1\right\}, & n \text{ even}.\end{cases} \tag{E2}$$

$w[(k_1/2)x;\vartheta]d[(k_1/2)x;\vartheta]$:

$$A_n(\vartheta)=\begin{cases}\dfrac{1}{\pi}\vartheta, & n=0\\ -\dfrac{1}{n\pi}\sin\left[n\left(\dfrac{\pi}{2}-\vartheta\right)\right], & n \text{ even}\\ -\dfrac{1}{n\pi}\left\{\sin\left[n\left(\dfrac{\pi}{2}-\vartheta\right)\right]+i\right\}, & n=\text{odd}.\end{cases} \tag{E3}$$

$\tilde{m}_0(x)$:

$$A_n(\vartheta)=\begin{cases}0, & n=0\\ \pm\left\{\dfrac{i}{\pi}\vartheta-\dfrac{i}{n\pi}\sin\left[2\left(\dfrac{\pi}{2}-\vartheta\right)\right]\right\}, & n=\pm 1\\ \dfrac{i}{(n-1)\pi}\sin\left[(n-1)\left(\dfrac{\pi}{2}-\vartheta\right)\right]-\dfrac{i}{(n+1)\pi}\sin\left[(n+1)\left(\dfrac{\pi}{2}-\vartheta\right)\right] & \text{otherwise}.\end{cases} \tag{E4}$$

$\tilde{m}_1(x)$:

$$A_n(\rho,\sigma,\vartheta)=\sum_m\left(\tilde{J}_{2m}(\rho,\sigma)+\frac{1}{2}[\tilde{J}_{2m-1}(\rho,\sigma)+\tilde{J}_{2m+1}(\rho,\sigma)]\right)A^d_{n-2m+2}$$
$$+\sum_m\left(\tilde{J}_{2m+1}(\rho,\sigma)+\frac{1}{2}[\tilde{J}_{2m}(\rho,\sigma)+\tilde{J}_{2m+2}(\rho,\sigma)]\right)A^{w\cdot d}_{n-2m+1}. \tag{E5}$$

$|\tilde{m}_1(x)|$:

$$A_n(\vartheta)=\begin{cases}\dfrac{1}{2}-\dfrac{1}{\pi}\sin\left(\dfrac{\pi}{2}-\vartheta\right), & n=0\\ \mp\dfrac{i}{\pi}\cos\left(\dfrac{\pi}{2}-\vartheta\right)+\dfrac{\vartheta}{2\pi}-\dfrac{1}{4\pi}\sin\left[2\left(\dfrac{\pi}{2}-\vartheta\right)\right], & n=\pm 1\\ -\dfrac{i}{\pi n}\cos\left[n\left(\dfrac{\pi}{2}-\vartheta\right)\right]-\dfrac{1}{\pi(n-1)}\sin\left[(n-1)\left(\dfrac{\pi}{2}-\vartheta\right)\right]\\ -\dfrac{1}{\pi(n+1)}\sin\left[(n+1)\left(\dfrac{\pi}{2}-\vartheta\right)\right]\end{cases}$$
$$+\begin{cases}\dfrac{i}{\pi}\left(\dfrac{1}{n}-\dfrac{1}{n-1}-\dfrac{1}{n+1}\right), & n \text{ even}\\ 0, & n \text{ odd.}\end{cases} \tag{E6}$$

$\widetilde{m}_0(x)|\widetilde{m}_1(x)|$:

$$\begin{aligned}A_n(\vartheta)=\frac{1}{4}\Bigg\{&\frac{1}{\pi}\Bigg[\frac{-1}{n-2}\left\{\cos\left[(n-2)\left(\frac{\pi}{2}-\vartheta\right)\right]-\delta_{n,\text{even}}\right\} && (n\neq 2)\\ &+\frac{1}{n+2}\left\{\cos\left[(n+2)\left(\frac{\pi}{2}-\vartheta\right)\right]-\delta_{n,\text{even}}\right\} && (n\neq -2)\\ &+\frac{2}{n-1}\left\{i\,\sin\left[(n-1)\left(\frac{\pi}{2}-\vartheta\right)\right]-\delta_{n,\text{even}}\right\} && (n\neq 1)\\ &-\frac{2}{n+1}\left\{i\,\sin\left[(n+1)\left(\frac{\pi}{2}-\vartheta\right)\right]-\delta_{n,\text{even}}\right\}\Bigg] && (n\neq -1)\\ &+\frac{1}{2i}(\delta_{n,2}-\delta_{n,-2})+\frac{2\vartheta}{i\pi}(\delta_{n,1}-\delta_{n,-1})\Bigg\},\end{aligned}$$

$$\delta_{n,\text{even}}\equiv\begin{cases}0, & n \text{ odd},\\ 1, & n \text{ even}.\end{cases} \tag{E7}$$

[1] P. Coullet, L. Gil, and J. Lega, Phys. Rev. Lett. **62**, 1619 (1989).

[2] Y. Pomeau, Physica D **23**, 3 (1986); P. Manneville, in *Nonlinear Evolution of Spatio-Temporal Structures in Dissipative Continuous Systems*, edited by F. H. Busse and L. Kramer (Plenum, New York, 1990).

[3] B. Nicolaenko, B. Schaurer, and R. Temam, Physica D **16**, 155 (1985).

[4] B. I. Shraiman, Phys. Rev. Lett. **57**, 325 (1986).

[5] S. Zaleski, Physica D **34**, 427 (1989).

[6] P. C. Hohenberg and B. I. Shraiman, Physica D **37**, 109 (1989).

[7] Z. S. She, U. Frisch, and O. Thual, in *Macroscopic Modelling of Turbulent Flows*, edited by U. Frisch, J. B. Keller, G. Papanicolaou, and O. Pironneau, Lecture Notes in Physics Vol. 230 (Springer, Berlin, 1986), p. 36; U. Frisch, Z. S. She, and O. Thual, J. Fluid Mech. **168**, 221 (1986).

[8] P. Manneville, Phys. Lett. **84A**, 129 (1981).

[9] I. Procaccia, M. H. Jensen, V. S. L'vov, K. Sneppen, and R. Zeitak, Phys. Rev. A **46**, 3220 (1992).

[10] J. M. Hyman, B. Nicolaenko, and S. Zaleski, Physica D **23**, 265 (1986).

[11] J. M. Greene and J.-S. Kim, Physica D **33**, 99 (1988); M. S. Jolly, I. G. Kevrekidis, and E. S. Titi, *ibid.* **44**, 38 (1990).

[12] I. Procaccia, S. Thomae, and C. Tresser, Phys. Rev. A **35**, 1884 (1987).

[13] P. Kent and J. Elgin, Nonlinearity **5**, 899 (1992).

[14] A. Zippelius and E. D. Siggia, Phys. Fluids **26**, 2905 (1983).

[15] H. S. Greenside, M. C. Cross, and W. M. Coughran Jr., Phys. Rev. Lett. **60**, 2269 (1988).

[16] A. Pocheau, in *Propagation in Systems Far from Equilibrium*, edited by J. Wesfreid, H. Brand, P. Manneville, G. Albinet, and N. Boccara (Springer-Verlag, Berlin, 1988).

[17] V. Croquette, Contemp. Phys. **30**, 153 (1989).

[18] P. Collet, J.-P. Eckmann, H. Epstein, and J. Stubbe, Phys. Rev. D **67**, 321 (1993).

[19] A. P. Hooper and R. Grimshaw, Wave Motion **10**, 405 (1988).

[20] D. Michelson, Physica D **19**, 89 (1986).

[21] O. Thual, U. Frisch, and M. Hénon, J. Phys. (Paris) **46**, 1485 (1985).

[22] G. Goren, Ph.D. thesis, Weizmann Institute of Science, 1995 (unpublished).

[23] We use the conventional notation for continued fractions: $[a_0,a_1,a_2,\ldots]=1/\{a_0+1/[a_1+1/(a_2+\ldots)]\}$.

[24] M. J. Feigenbaum, L. P. Kadanoff, and S. J. Shenker, Physica D **5**, 370 (1982); S. J. Shenker, *ibid.* **5**, 405 (1982).

[25] M. H. Jensen, P. Bak, and T. Bohr, Phys. Rev. A **30**, 1960 (1984); T. Bohr, P. Bak, and M. H. Jensen, *ibid.* **30**, 1970 (1984).

[26] H. A. Lauwerier, in *Chaos*, edited by A. V. Holden (Manchester University Press, Manchester, 1986).

[27] D. Ruelle and F. Takens, Commun. Math. Phys. **20**, 167 (1971); **23**, 343 (1971).

[28] S. E. Newhouse, D. Ruelle, and F. Takens, Commun. Math. Phys. **64**, 35 (1978).

[29] W. Eckhaus, *Studies in Nonlinear Stability Theory* (Springer, New York, 1965).

[30] Y. Kuramoto, Prog. Theor. Phys. **71**, 1182 (1984).

[31] B. Janiaud, A. Pumir, D. Bensimon, V. Croquette, H. Richter, and L. Kramer, Physica D **55**, 269 (1992).

[32] H. Sakaguchi, Prog. Theor. Phys. **84**, 792 (1990).

[33] C. Grebogi, E. Ott, F. Romeiras, and J. A. Yorke, Phys. Rev. A **36**, 5365 (1987); C. Grebogi, E. Ott, and J. A. Yorke, Physica D **24**, 243 (1987).

[34] J.-P. Eckmann and I. Procaccia, Nonlinearity **4**, 567 (1991); J.-P. Eckmann and I. Procaccia, Phys. Rev. Lett. **66**, 891 (1991); J.-P. Eckmann, G. Goren, and I. Procaccia, Phys. Rev. A **44**, R805 (1991).

[35] To find $m_1(x)$ we recorded the field $U(x,t)$ for $x \in [0,\mathrm{L})$, $t \in [0,\mathrm{T})$ and Fourier transformed it in space and time. Then $m_1(x)$ is $m_1(x) = \int_0^\infty dk\, e^{i(k-k_0)x} U(\omega_0,k)$, where ω_0 is the frequency of the periodic orbit.

[36] J. Moré, B. Garbow, and K. Hillstrom, User Guide for MINPACK-1, Argonne National Laboratory Report No. ANL 80-74 (unpublished).